Article

Tissue-resident macrophages provide a pro-tumorigenic niche to early NSCLC cells

https://doi.org/10.1038/s41586-021-03651-8

Received: 1 March 2020

Accepted: 18 May 2021

Published online: 16 June 2021

Check for updates

María Casanova-Acebes[1,2,3,19]✉, Erica Dalla[4,5,6,7,21], Andrew M. Leader[1,2,3,21], Jessica LeBerichel[1,2,3,21], Jovan Nikolic[8], Blanca M. Morales[9], Markus Brown[9], Christie Chang[1,2,3], Leanna Troncoso[1,2,3], Steven T. Chen[1,2,3], Ana Sastre-Perona[10,11], Matthew D. Park[1,2,3], Alexandra Tabachnikova[1,2,3], Maxime Dhainaut[2,3,12], Pauline Hamon[1,2,3], Barbara Maier[1,2,3,20], Catherine M. Sawai[13], Esperanza Agulló-Pascual[14], Markus Schober[10], Brian D. Brown[2,3,12,17], Boris Reizis[15], Thomas Marron[1,2,3,4,16], Ephraim Kenigsberg[2,17], Christine Moussion[9], Philippe Benaroch[8], Julio A. Aguirre-Ghiso[1,2,3,4,5,6,7,22] & Miriam Merad[1,2,3,18,22]✉

Macrophages have a key role in shaping the tumour microenvironment (TME), tumour immunity and response to immunotherapy, which makes them an important target for cancer treatment[1,2]. However, modulating macrophages has proved extremely difficult, as we still lack a complete understanding of the molecular and functional diversity of the tumour macrophage compartment. Macrophages arise from two distinct lineages. Tissue-resident macrophages self-renew locally, independent of adult haematopoiesis[3–5], whereas short-lived monocyte-derived macrophages arise from adult haematopoietic stem cells, and accumulate mostly in inflamed lesions[1]. How these macrophage lineages contribute to the TME and cancer progression remains unclear. To explore the diversity of the macrophage compartment in human non-small cell lung carcinoma (NSCLC) lesions, here we performed single-cell RNA sequencing of tumour-associated leukocytes. We identified distinct populations of macrophages that were enriched in human and mouse lung tumours. Using lineage tracing, we discovered that these macrophage populations differ in origin and have a distinct temporal and spatial distribution in the TME. Tissue-resident macrophages accumulate close to tumour cells early during tumour formation to promote epithelial–mesenchymal transition and invasiveness in tumour cells, and they also induce a potent regulatory T cell response that protects tumour cells from adaptive immunity. Depletion of tissue-resident macrophages reduced the numbers and altered the phenotype of regulatory T cells, promoted the accumulation of $CD8^+$ T cells and reduced tumour invasiveness and growth. During tumour growth, tissue-resident macrophages became redistributed at the periphery of the TME, which becomes dominated by monocyte-derived macrophages in both mouse and human NSCLC. This study identifies the contribution of tissue-resident macrophages to early lung cancer and establishes them as a target for the prevention and treatment of early lung cancer lesions.

To analyse the components of macrophages that populate human NSCLC lesions, we made use of an existing single-cell RNA-seq (scRNA-seq) dataset that maps the $CD45^+$ leukocyte compartment of early-stage, treatment-naive human NSCLC lesions[6]. Unbiased RNA-based clustering using a previously reported algorithm[7] revealed multiple clusters of macrophages and monocytes (Fig. 1a). The clusters were broadly grouped into $CD14^+$ monocytes (defined by the expression of *CD14*, *VCAN* and *S100A12*, and termed 'group III') (Supplementary Table 1) and $CD16^+$ monocytes (defined by the expression of *FCGR3A* and the absence of *CD14* and other macrophage genes, and termed 'group IV') (Supplementary Table 1). We also identified several macrophage clusters that expressed canonical macrophage genes such as *MRC1*, *C1QA*, *CD68* and *APOE* and lacked a monocyte signature (Fig. 1a, Extended Data Fig. 1i, Supplementary Table 1). The macrophage clusters included a homogenous cluster (termed 'group I') expressing the transcription factor *PPARG*, which is known to control the ability of alveolar macrophages to clear surfactant protein[8]. This cluster also expressed high levels of the cell-cycle genes *MKI67* and *STMN1*, consistent with the self-renewal potential of tissue-resident macrophages (TRMs), as well as expressing *MARCO* and *MRC1* (Extended Data Fig. 1i, Supplementary Table 1). Alveolar macrophages are the TRMs of the lung, and thus we tentatively termed this cluster 'alveolar macrophages'. The remaining clusters were broadly classified as 'group II', because they lacked transcripts expressed by group I macrophages or monocytes (Supplementary Table 1).

A list of affiliations appears at the end of the paper.

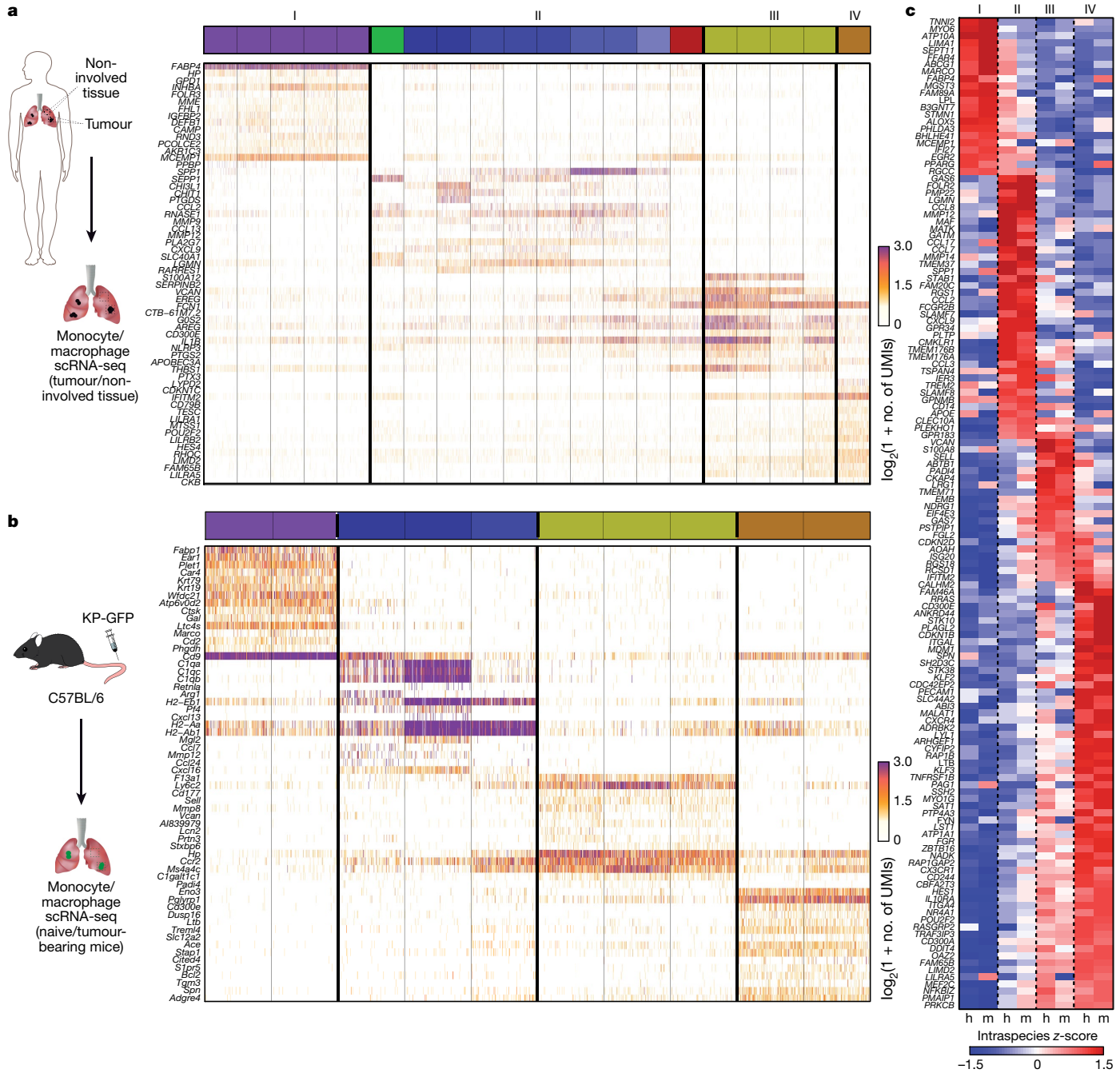

Fig. 1 | scRNA-seq of lineage-traced blood-derived macrophages reveals two ontogenically distinct populations of macrophages in NSCLC lesions. **a**, scRNA-seq data of human macrophage and monocyte clusters from tumour samples and non-involved lung samples from 35 patients with early-stage NSCLC. Group I and group II were annotated as macrophage clusters, group III as CD14^{+} monocytes and group IV as non-classical monocytes. Heat maps show unique molecular identifier (UMI) counts of selected genes in myeloid clusters after evenly down-sampling to 2,000 UMIs per cell. **b**, scRNA-seq data of macrophages and monocytes in two pooled naive and two pooled tumour-bearing mice in an orthotopic mouse model of NSCLC in which mice were injected intravenously with KP cells genetically labelled with GFP. Clusters are down-sampled to show a maximum of 200 cells per cluster. **c**, Orthology signature in human (h) and mouse (m) for NSCLC tumour-associated macrophages and monocytes (groups I–IV).

Ontogeny of NSCLC-associated macrophage programs

To examine whether mice models could provide an informative setting for studying the myeloid clusters identified in human NSCLC, we searched for similar myeloid cellular compartments in a preclinical mouse model of lung adenocarcinoma. We used an orthotopic model in which tail vein injection of *Kras*^{G12D} and *p53*-deficient (KP) lung epithelial cells genetically labelled with GFP leads to mouse lung adenocarcinoma lesions that resemble human NSCLC lesions[9] (Fig. 1b). Similar to our findings in human lesions, scRNA-seq of mouse tumours revealed four groups of clusters comprising monocytes and macrophages. Group I expressed *Pparg*, *Mrc1*, *Marco*, *Siglecf*, *Cd2 and Siglec1*, whereas group II was defined by high expression of *C1q*, *Mafb*, *Arg1*, *Mgl2* and *Trem2*. Group III was defined as Ly6C^{hi} monocytes on the basis of the expression of *Ccr2*, *Ly6c2* and *F13a1*, and group IV as Ly6C^{lo} monocytes on the basis of the expression of *Cx3cr1*, *Nr4a1*, *Pglyrp1*, *Eno3* and *Ace*, and the absence of *Ccr2* and *Ly6c2* expression (Fig. 1b, Extended Data Fig. 1h, Supplementary Table 2). These cluster

annotations were reinforced by correlation with previously described clusters[10] (Extended Data Fig. 1g).

Although previous cross-species analyses between lung macrophage subsets have shown that the majority of genes expressed by analogous subsets are not conserved[10,11], we set out to identify the gene modules that are conserved despite the evident species differences (Fig. 1c). Mouse and human group I clusters shared many genes, including high expression of scavenger receptors (*MARCO* and *SIGLEC1*), cell-cycle genes (*STMN1* and *TUBA1B*)—suggesting self-renewal potential—and the transcription factor *PPARG*. Mouse and human group II clusters also shared many genes, including genes associated with lipid metabolism (*APOE*, *TREM2*, *SPP1* and *GPNMB*) as well as monocyte-identity genes (*CCR2* and *CD14*). The mouse group III cluster aligned with the human $CD14^+$ monocytes, and the mouse group IV cluster aligned with human $CD16^+$ monocytes (Fig. 1c, Extended Data Fig. 1h, i).

The identification of homologous macrophage phenotypes in humans and mice provides a unique opportunity to examine the lineage origin of the tumour-associated macrophage clusters. To distinguish between adult monocyte-derived macrophages (MDMs), which are produced in the bone marrow, and self-maintained TRMs, we fate-mapped cells expressing MAP17, a molecule that is expressed on low-cycling adult haematopoietic stem cells (HSCs) but absent from embryonic HSCs (Extended Data Figs. 1a, b, 2a), using tamoxifen-inducible *Map17-creER* transgenic mice crossed with the *Rosa26-LSL-tdTomato* strain (*Map17*$^{creER/+}$*R26tdTom*) as described previously[12]. Six months after the injection of tamoxifen into non-tumour-bearing *Map17*$^{creER/+}$*R26tdTom* mice, we observed the efficient labelling of adult HSC progeny, including circulating and lung monocytes, whereas the majority of lung TRMs (also called alveolar macrophages) remained unlabelled—consistent with previous data showing that lung TRMs self-renew locally independent of adult haematopoiesis[4,12] (Extended Data Fig. 2b). To determine the ontogeny of the tumour-associated macrophage clusters, we injected KP tumour cells into *Map17*$^{creER/+}$*R26tdTom* mice once maximal labelling of circulating monocytes was reached (that is, six months after tamoxifen injection). Four weeks after KP injection, mice were euthanized and tumour-associated myeloid cells that either expressed ($Tomato^+$) or lacked ($Tomato^-$) the genetic label were purified and analysed by scRNA-seq (Extended Data Fig. 1a). We found that although many labelled cells mapped to most of the scRNA-seq cluster groups, the group I cluster was strongly depleted of $Tomato^+$ cells (Extended Data Fig. 2c). Similar results were obtained using a different model in which adult bone marrow myeloid progenitors were genetically fate-mapped using Tam-inducible *Cx3cr1-creER* transgenic mice crossed with *Rosa26-LSL-YFP* mice (*Cx3cr1*$^{creER/+}$*R26YFP*)[13]. KP cells were injected into tamoxifen-treated *Cx3cr1*$^{creER/+}$*R26YFP* mice and four weeks later, YFP^+ and YFP^- tumour-associated myeloid cells were isolated for scRNA-seq. Profiling of YFP^+ and YFP^- cells revealed that—similar to the results obtained in *Map17*$^{creER/+}$*R26tdTom* mice—group II, III and IV clusters contained many YFP^+ labelled cells, whereas the group I cluster was depleted of YFP^+ cells (Extended Data Figs. 1c, d, 2d–f).

These results suggest that the tumour-associated group I cluster in mice and its homologous cluster in humans arise from the TRM lineage, independent of adult HSCs, whereas all other clusters are derived from adult haematopoiesis, probably through a monocyte intermediate. We therefore named the group I cluster 'TRMs', and renamed the group II clusters to 'MDMs'. Our findings also reveal that blood-circulating myeloid progenitors and monocytes do not give rise to TRMs even in advanced tumour lesions, and that TRMs and MDMs cohabit the TME throughout tumour growth as observed in human lesions.

To further investigate whether the group I molecular signature that was identified in human NSCLC lesions refers to TRMs (alveolar macrophages), we leveraged data from two previous reports: inDrop-based scRNA-seq data from seven NSCLC tumours[10], and a list of alveolar macrophage transcripts identified by bulk RNA-seq of purified $SSC^{hi}CD14^-HLADR^+CD43^+$ alveolar macrophages isolated from bronchoalveolar lavages[11]. Correlation analyses confirmed that group I could also be identified in a distinct dataset of human NSCLC lesions and resembled the signature of purified human alveolar macrophages (Extended Data Fig. 1e–g). Together, our fate-mapping studies, cross-species analysis and mining of public datasets helped us to establish the molecular signature of TRMs in human lung cancer lesions and distinguish them from blood-derived macrophage clusters.

Spatial distribution of NSCLC macrophage programs

The identification of distinguishable molecular features of ontogenically distinct tumour-associated macrophages enabled us to differentiate TRMs in mice and human tumour lesions on the basis of their phenotype. Notably, we found that there was a marked reduction in the number of TRMs in both mouse and human tumours compared to normal lung tissues, whereas MDMs dominated advanced tumour lesions (Fig. 2a, Extended Data Fig. 3c). To understand why TRMs were reduced in tumour lesions, we measured the spatial interactions of TRMs with tumour cells over time during tumour expansion (Fig. 2b). We found that tumour cells localized close to TRMs up to day 15 after tumour seeding, before redistributing to the periphery of tumour lesions, resembling human granuloma lesions[14] (Fig. 2c, Extended Data Fig. 1j). A similar redistribution of TRMs was found in a genetically engineered mouse model of NSCLC[15] (Extended Data Fig. 3a, e) in which the instillation of adenovirus-expressing Cre (SPC-Cre) in transgenic KP mice induces NSCLC formation[16], and in human NSCLC lesions (Extended Data Fig. 3f, g).

Molecular changes in TRMs after NSCLC seeding

The close proximity of mouse TRMs and tumour cells that we observed in early lesions suggested that TRMs might have a role in shaping the early stages of tumour onset. To measure the response of TRMs to tumour cell seeding, we used bulk RNA-seq to profile TRMs isolated from early (day 15) or advanced (day 30) tumour lesions or from healthy control lung tissue (Extended Data Fig. 1k). We identified 1,670 differentially expressed genes (DEGs) between TRMs isolated from tumour-bearing lungs compared to TRMs from healthy control lungs (day 30, $P < 0.05$; Supplementary Table 3). Among them, 1,322 DEGs were induced in early lesions (Extended Data Fig. 4a). Early tumour TRMs expressed genes encoding peptidases (*Mmp12*, *Mmp14* and *Adamdec1*), integrin-binding molecules (*Tspan4*), major histocompatibility complex (MHC) class II molecules (*H2-M2*, *H2-AA*, *H2-AB1* and *H2-Q7*) and T cell chemoattractants (*Ccl17* and *Cxcl9*), and showed a significant downregulation in the expression of *Il1b* transcripts and genes encoding inflammasome mediators (*Nlrp1b*), negative regulators of the WNT signalling pathway (*Amer2*) and cell adhesion and migration molecules (*Ripor2*, *Dgkg*, *Fmnl3*, *Rasgrp4*, *Fmn1* and *Akap5*) (Extended Data Fig. 4a, b). To further explore the transcriptional responses of TRMs to early tumour cues, we measured TRM genome-wide chromatin accessibility using ATAC–seq (assay for transposase-accessible chromatin using sequencing). We found minimal changes in chromatin accessibility in tumour-associated TRMs compared to healthy control lungs (Extended Data Fig. 4c), consistent with the fact that TRMs are heavily imprinted by the tissue microenvironment in which they reside. Most enhanced chromatin accessibility changes occurred early during tumour progression (Extended Data Fig. 4c, Supplementary Table 4) and included coding regions for the proteases *Mmp12* and *Mmp13*. Genes encoding MHC class II molecules remained open throughout tumour progression (Extended Data Fig. 4d), whereas reduced chromatin accessibility was seen for gene-coding regions of *Ripor2* and *Dgkg*, which are known for their roles in cell migration and biosynthetic processes (Extended Data Figs. 2b, 4e). Together, our results suggest that TRMs minimally alter their transcriptional and epigenetic landscapes in response to

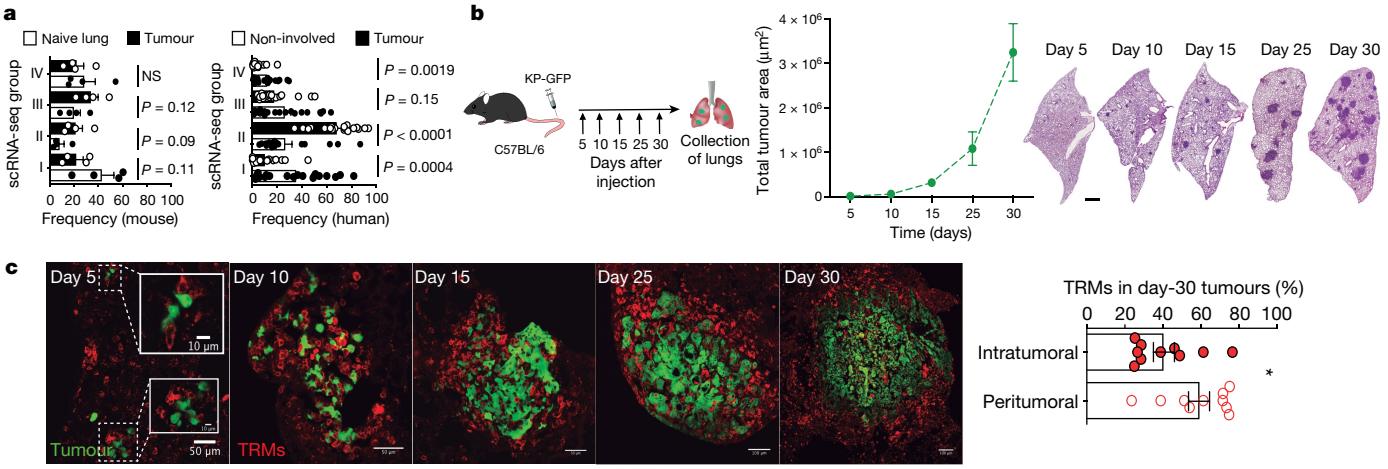

Fig. 2 | TRMs localize in close proximity to tumour cells after seeding and enhance their antigen presentation and tissue remodelling programs in response to tumour cues. a, Frequency of scRNA-seq groups in lungs from naive and tumour-bearing mice (left, $n = 4$ experiments with two pooled naive and two pooled tumour-bearing mice per experiment) and in human NSCLC tumours and adjacent non-involved lung tissue (right, 19 paired non-involved and tumour). The cell-type frequencies observed in the scRNA-seq mouse samples were proportionally weighted according to the labelling frequencies determined from fluorescence-activated cell sorting (FACS). Unpaired two-tailed *t*-test. NS, not significant. Data are mean ± s.e.m. **b**, Longitudinal analysis in an orthotopic mouse model of NSCLC (left). Graph (middle) shows tumour growth over time, and images (right) show tumour foci stained with haematoxylin and eosin ($n = 3$ day 5; $n = 4$ day 10; $n = 4$ day 15; $n = 3$ day 25; $n = 8$ day 30). Scale bar, 10 mm. **c**, Left, confocal imaging of tumour lesions (KP, green) and TRMs (MRC1, red) at different time points after the injection of KP cells. Scale bar, 50 μm (main images, day 5, 10 and 15); 100 μm (main images, days 25 and 30); 10 μm (insets). Right, quantification of the distribution of TRMs in advanced tumour lesions (day 30; $n = 4$ mice, 10 tumours). Unpaired two-tailed *t*-test; $^*P < 0.05$. Data are mean ± s.e.m.

early tumour seeding, and that most of the transcriptional changes are related to antigen presentation and tissue remodelling.

Contribution of TRMs to early tumour progression

To determine whether the interactions of tumour cells with TRMs affected their cellular behaviour, we cultured KP cells in a three-dimensional (3D) spheroid system alone or with purified TRMs (Extended Data Fig. 5c) or bone marrow monocytes, which give rise to MDMs in tissues (Fig. 3a). Tumour cells cultured with TRMs expressed a distinct molecular program associated with tumour cell migration, epithelial–mesenchymal transition (EMT) and lipid metabolic changes (Fig. 3b, Extended Data Fig. 5a, b, e, Supplementary Table 5), whereas KP cells co-cultured with bone marrow monocytes mainly expressed genes that control cell-cycle progression and the DNA replication response (Fig. 3c, Extended Data Fig. 5b, Supplementary Table 5). Notably, KP cells co-cultured with TRMs also exhibited an increase in the dispersion of tumour cells over time, compared to KP cells cultured alone or with bone marrow monocytes (Fig. 3d), suggesting that TRMs contribute to tumour invasiveness and tissue remodelling, as observed during EMT. EMT is a physiological program that allows epithelial cells to acquire mesenchymal and invasiveness properties[17] during embryogenesis and wound repair[18] and is known to promote tumour invasiveness and metastasis[19–21]. EMT is associated with reduced expression of E-cadherin, altered epithelial cell junctions and the acquisition of an invasive phenotype[22], and is driven by the activation of β-catenin and by the transcription factor TWIST1, among others[23,24]. Accordingly, we found that after co-culture with TRMs, tumour cells showed a significant reduction in their protein expression of E-cadherin, compared to KP cells cultured alone or with bone marrow monocytes or purified tumour-associated MDMs (Fig. 3e, f, Extended Data Fig. 5d). Using a 3D-matrigel assay to further examine the ability of macrophages to promote tumour cell invasiveness and expansion, we found that KP cells cultured with TRMs formed invasive protrusions, consistent with an EMT program (Fig. 3g, Extended Data Fig. 5h, i, Supplementary Video 1), whereas KP cells that were cultured with tumour-associated MDMs or bone marrow monocytes formed colonies with an increased frequency and size and did not form invasive protrusions (Extended Data Fig. 5f, g, j, k, Supplementary Video 2). The ability of TRMs to promote invasiveness in KP cells was further established through a transwell migration assay using conditioned medium derived from tumour TRMs (Fig. 3h). In addition, tumour cells that formed in the absence of TRMs expressed reduced levels of the EMT-associated transcription factor TWIST1 (Fig. 3i). Together, these results establish that TRMs drive a tissue remodelling program and promote tumour cell invasiveness during the initial stages of tumour progression.

Epigenetic and transcriptional profiling also revealed that tumour-associated TRMs upregulated their expression of MHC class II genes in early NSCLC lesions, suggesting that these TRMs might contribute to the presentation of antigens to $CD4^+$ T cells (Extended Data Fig. 4a, d). We previously found that the most striking difference between the immune cell composition of tumour lesions in human NSCLC compared to adjacent healthy tissues was the increased frequency of regulatory T (T_{reg}) cells[25]. Of note, molecules such as VEGFA and the urokinase-type plasminogen activator (uPA, encoded by *Plau*), which are expressed by KP cells in the presence of TRMs (Fig. 3b), have been linked to an immunosuppressive microenvironment that is related to the differentiation of T_{reg} cells[26–28].

To measure whether tumour-associated macrophages from independent hematopoietic origin differently contributed to the regulation of the pool of tumour-associated T_{reg} cells, we measured the capacity of purified tumour-associated MDMs and TRMs to induce the differentiation of T_{reg} cells ex vivo. We found that both compartments were similarly efficient at promoting the differentiation of naive T cells into T_{reg} cells, but that TRMs were uniquely able to enhance the expression of CD73 and CTLA-4 on differentiated T_{reg} cells compared to MDMs (Extended Data Fig. 6a). Imaging of cleared early KP tumours revealed that T_{reg} cells established close contacts with TRMs in tumour lesions, and that the accumulation of T_{reg} cells correlated with tumour growth in mice (Fig. 4b–d). We reasoned that TRMs might contribute to the early expansion of T_{reg} cells, as reflected by the increased proliferation and frequency of T_{reg} cells in early tumour lesions (Fig. 4a) and our findings that tumour-associated TRMs expressed high levels of *Ccl17* and *Tgfb1*, which are known to

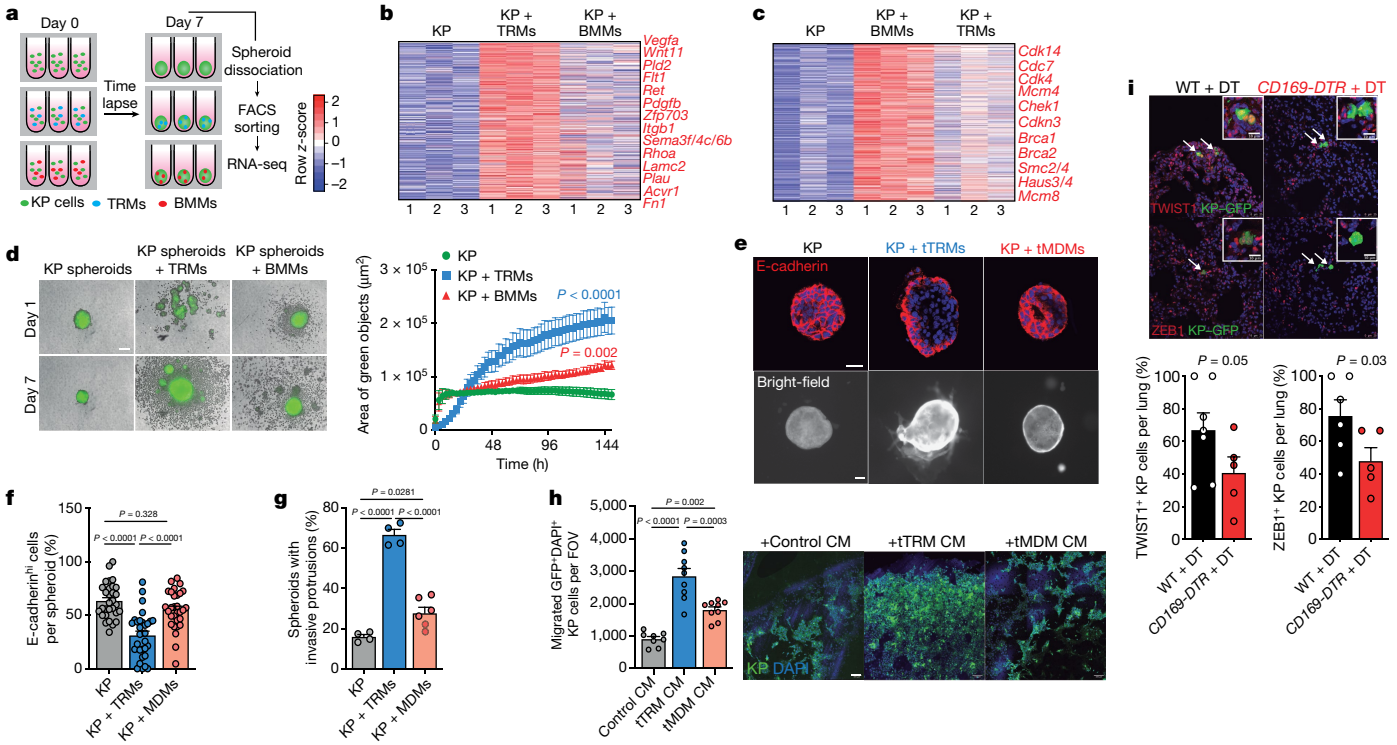

Fig. 3 | TRMs induce NSCLC cells to undergo EMT and promote tumour cell invasiveness. a, Scheme of KP spheroids co-cultured with TRMs or bone marrow monocytes (BMMs). **b**, Heat map showing *z*-scores of uniquely DEGs in KP spheroids with TRMs. Upregulated genes are shown in red ($P < 0.05$, $\log_2$(expression in TRMs/expression in KP spheroids) > 1. KP cells were sorted as singlets, DAPI$^-$CD45$^-$GFP$^+$. **c**, Heat map showing *z*-scores of uniquely DEGs in KP spheroids with bone marrow monocytes. **d**, Left, live spheroid imaging. Right, the GFP signal was quantified over time and the area of dispersed GFP objects (cells) was plotted. One-way ANOVA; $^{**}P < 0.01$, $^{****}P < 0.0001$. Data are mean ± s.e.m. Scale bar, 200 μm. Results are representative of five pooled independent experiments. **e**, Representative confocal images of E-cadherin (red) and bright-field images (for invasive protrusions) of KP alone or with tumour-associated TRMs (tTRMs) or tumour-associated MDMs (tMDMs). Scale bars, 25 μm (fluorescence images; top); 100 μm (bright-field images; bottom). Images are representative of two independent experiments with similar results. **f**, Frequency of E-cadherin^{hi} cells per spheroid in KP cells alone or with tTRMs or tMDMs. One-way ANOVA with Tukey's test for multiple comparisons. Data are mean ± s.e.m. and are representative of two pooled independent experiments. **g**, Frequency of invasive spheroids in KP cells alone or with tTRMs or tMDMs. One-way ANOVA. Data are mean ± s.e.m. and are representative of two pooled independent experiments. **h**, Right, representative images of a transwell migration assay of KP cells (green, nuclei in blue (DAPI)) with control conditioned medium (CM), tTRM conditioned medium and tMDM conditioned medium. Scale bar, 100 μm. Left, the number of migrated GFP$^+$DAPI$^+$ cells per field of view (FOV) was quantified after 18 h. One-way ANOVA. Data are mean ± s.e.m. and are representative of two independent experiments. **i**, Left, confocal imaging of TWIST1 (red) and ZEB1 (red) GFP-expressing KP cells in TRM-sufficient (wild type; WT) and TRM-deficient (*CD169-DTR*) mice, five days after injection with diphtheria toxin (DT). Orange indicates co-expression of TWIST1 or ZEB1 and GFP. Right, the frequency of TWIST1$^+$ and ZEB1$^+$ KP cells is quantified for WT + DT (black) and *CD169-DTR* + DT (red). Unpaired one-tailed *t*-test. Data are mean ± s.e.m. and are representative of two independent experiments.

contribute to the recruitment, differentiation and expansion of T_{reg} cells[29–31] (Extended Data Fig. 6c).

To directly determine whether TRMs promoted the early expansion of T_{reg} cells, we tested whether the depletion of TRMs affected the accumulation of T_{reg} cells in tumours. To deplete TRMs without affecting MDMs, we used a deleter mouse line in which the diphtheria toxin receptor (DTR) is expressed under the control of the CD169 promoter (*CD169-DTR* mice), on the basis of the results of our scRNA-seq analysis of fate-mapped macrophages that showed that *Siglec1* (CD169) was expressed at higher levels in TRMs than in MDMs (Extended Data Fig. 1h, j, k). Using *Ms4a3-tdTom* reporter mice[32] to trace the progeny of monocytes in KP lung tumours, we confirmed that CD169 expression was negligible in monocytes or MDMs that populate naive lungs and early tumour lesions (Extended Data Fig. 6e). Notably, intranasal instillation of diphtheria toxin into *CD169-DTR* mice depleted TRMs specifically, in the lungs, without affecting other myeloid cell populations—establishing that *CD169-DTR* mice treated with diphtheria toxin could be used to measure the functional specialization of TRMs in early tumour lesions (Extended Data Fig. 6d, f).

Thus, *CD169-DTR* mice were injected with diphtheria toxin before tumour implantation, and tumour cell engraftment and the number and phenotype of T_{reg} cells were measured at different times during tumour progression (Fig. 4e). We found that depletion of TRMs not only resulted in a reduction in the number of T_{reg} cells in early lesions (Extended Data Fig. 6b), but also altered the molecular programs of T_{reg} cells, leading to reduced expression of CTLA-4 and CD73 (Extended Data Fig. 6b)—consistent with our in vitro results (Extended Data Fig. 6a). This effect was restricted to the tumours, as no changes in T_{reg} cells were observed in tumour-draining lymph nodes or in the spleen (Extended Data Fig. 6g). Notably, depletion of TRMs reduced the size of tumours without affecting the number of tumour lesions (Fig. 4f). Reduced tumour burden was not a result of impaired tumour cell seeding, as similar numbers of KP cells were recovered from the lungs of TRM-sufficient or -deficient mice 24 hours after injection (Extended Data Fig. 6h). Tumour lesions in TRM-depleted mice had an increased number of cleaved caspase-3-positive (CC3$^+$) cells and slow-cycling p27$^+$ cells compared with those in TRM-sufficient mice (Extended Data Fig. 6i), suggesting impaired survival and growth potential. We also found increases in the total number of CD3$^+$ T cells (Fig. 4h), the total

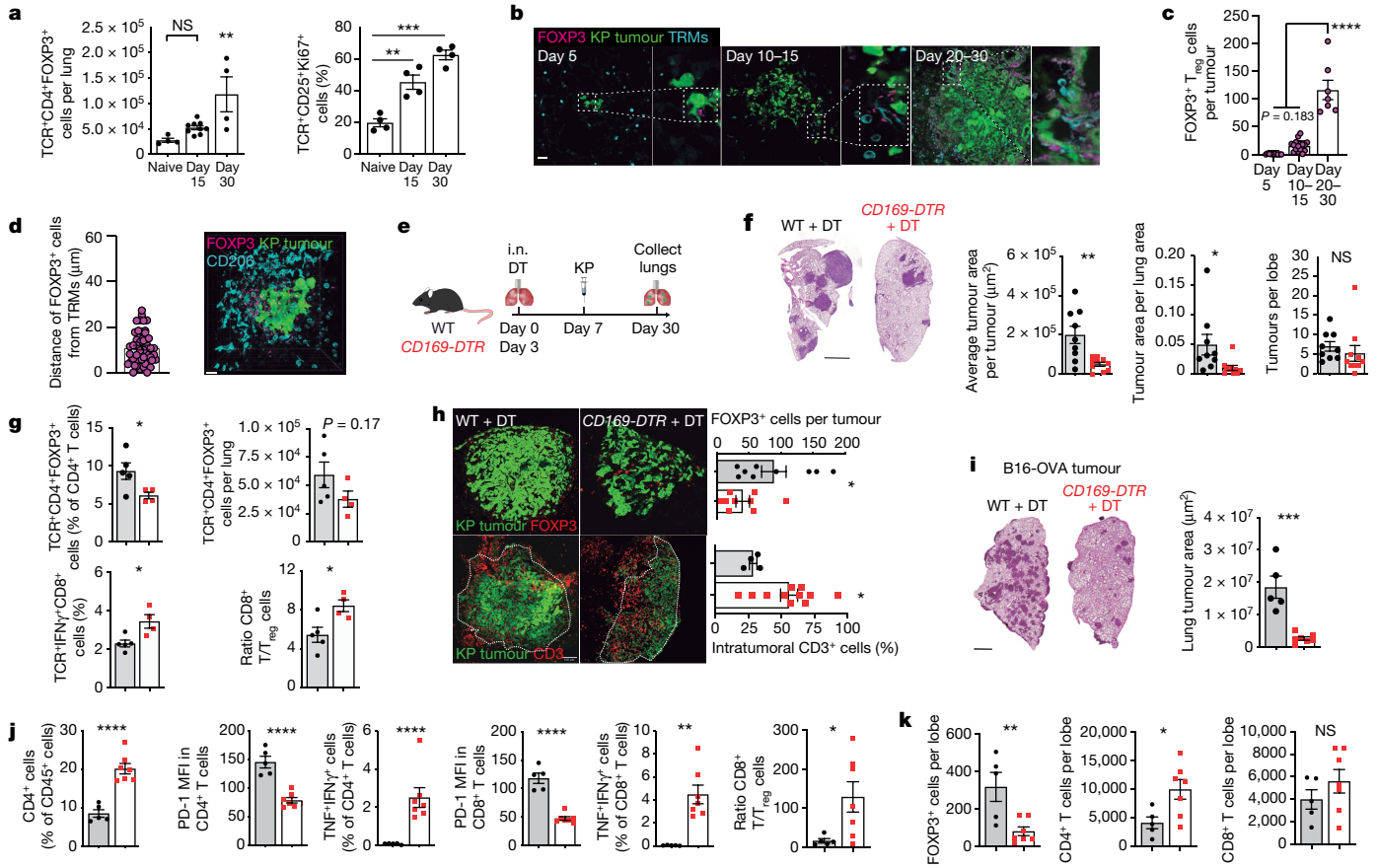

Fig. 4 | Depletion of TRMs before tumour engraftment leads to reduced tumour burden and enhances T cell infiltration. a, Number (left) and frequency (right) of T_{reg} cells in naive and KP lungs (left: $n = 4$ naive, $n = 9$ day 15 KP, $n = 4$ day 30 KP; right (proliferative T_{reg} cells): $n = 4$ mice per time). T_{reg} cells: $DAPI^-CD45^+TCR^+CD4^+FOXP3^+$; proliferative T_{reg} cells: $Ki67^+DAPI^-CD45^+TCR^+CD4^+CD25^+$. One-way ANOVA with Bonferroni's test; left, NS, $P = 0.472$, $^{**}P = 0.0037$; right, $^{**}P = 0.0011$, $^{***}P < 0.0001$. Data are mean ± s.e.m. **b**, Temporal location of TRMs ($MRC1^+$, blue) and T_{reg} cells ($FOXP3^+$, magenta). KP cells are shown in green. Scale bar, 30 μm. Images are representative of a single longitudinal experiment. **c**, Quantification of T_{reg} cells from **b**. Seven to ten FOVs per time point. One-way ANOVA with Bonferroni's test; $^{****}P < 0.0001$. Data are mean ± s.e.m. **d**, Mean distance of T_{reg} cells to TRMs (at day 15). Scale bar, 15 μm. **e**, Depletion of TRMs using intranasal (i.n.) instillation of diptheria toxin (days 0 and 3) and orthotopic intravenous (i.v.) injection of KP cells. **f**, Tumour burden in wild-type (black) or TRM-depleted (*CD169-DTR*; red) mice treated with diphtheria toxin ($n = 9$ WT + DT, $n = 10$ *CD169-DTR* + DT. Unpaired two-tailed *t*-test; $^{**}P = 0.0028$, $^{*}P = 0.0345$, NS, $P = 0.46$. Data are mean ± s.e.m. Scale bar, 2 mm. **g**, Quantification of $TCR^+CD4^+FOXP3^+$ T_{reg} cells, $TCR^+IFN\gamma^+TNF^+CD8^+$ cells and ratio of $CD8^+$ T cells/T_{reg} cells in tumour-bearing wild-type (black) or TRM-depleted (red) mice. Unpaired two-tailed *t*-test; $^{*}P = 0.041$ (percentage $TCR^+CD4^+FOXP3^+$ T_{reg} cells), $^{*}P = 0.016$ ($TCR^+IFN\gamma^+TNF^+CD8^+$ cells), $^{*}P = 0.022$ (ratio $CD8^+$ T cells/T_{reg} cells). Data are mean ± s.e.m. from two independent experiments. **h**, Imaging and quantification of tumour-infiltrating T_{reg} cells and $CD3^+$ T cells in TRM-sufficient (black) and TRM-deficient (red) mice ($n = 9$ mice). White dotted lines mark the tumour area. Unpaired two-tailed *t*-test; $^{*}P = 0.041$ ($FOXP3^+$ T_{reg} cells), $^{*}P = 0.028$ ($CD3^+$ T cells). Data are mean ± s.e.m. Two independent experiments. **i**, Tumour burden in B16-F10/OVA mice ($n = 5$ WT + DT (black), $n = 7$ *CD169-DTR* + DT (red)). Unpaired two-tailed *t*-test; $^{***}P = 0.0003$. Data are mean ± s.e.m. from two independent experiments. Scale bar, 1 mm. **j**, Relative frequency of $CD4^+$ cells, mean fluorescent intensity (MFI) of PD-1 in $CD4^+$ and $CD8^+$ T cells, and quantification of $TNF^+IFN\gamma^+$ cells in $CD4^+$and $CD8^+$ T cells in B16-F10-BFP/OVA wild-type (black) and TRM-depleted (red) mice ($n = 5$ and $n = 7$, respectively). Unpaired two-tailed *t*-test; $^{****}P < 0.0001$, $^{**}P = 0.001$, $^{*}P = 0.0375$. Data are mean ± s.e.m. Two independent experiments. **k**, Quantification of tumour-infiltrating T_{reg} cells and $CD4^+$ and $CD8^+$ T cells in the B16-OVA model ($n = 5$ WT + DT, $n = 7$ *CD169-DTR* + DT). Unpaired two-tailed *t*-test; $^{**}P = 0.0068$, $^{*}P = 0.025$, NS, $P = 0.2887$. Data are mean ± s.e.m. Two independent experiments.

number of $IFN\gamma^+TNF^+CD8^+$ T cells and the ratio of $CD8^+$ T cells to T_{reg} cells in tumour lesions in TRM-depleted mice compared to those of TRM-sufficient mice (Fig. 4g, h). A stronger effect on tumour growth was observed when TRMs were depleted in the more immunogenic B16-OVA model of metastatic melanoma (Fig. 4i). Of note, tumour reduction was not associated with an increase in OVA-antigen-specific OT-I or OT-II T cells (Extended Data Fig. 7a–d). However, we observed an expansion of IFNγ- and TNF-producing $CD4^+$ and $CD8^+$ effector T cells and a reduction of PD-1 expression in the total pool of $CD4^+$ and $CD8^+$ T cells (Fig. 4j). Similar to the KP model, depletion of TRMs led to a reduction in T_{reg} cells and an increase in the $CD8^+$ T cell/T_{reg} cell ratio (Fig. 4j, k). In contrast to early-stage tumour lesions, depletion of TRMs in established KP lesions (days 12–15) did not affect tumour burden, the T_{reg} compartment, the $CD8^+$ T cell/T_{reg} cell ratio or the number of $CD3^+$ tumour-infiltrating T cells (Extended Data Fig. 6j–m).

TRMs and MDMs coexist in early lung cancer lesions and retain a distinct phenotypic and molecular program even in late-stage tumours. Using imaging of the distribution of tumour macrophages, RNA-seq profiling of 3D co-cultures of tumour cells with TRMs, and conditional deleter mice to eliminate TRMs before tumour implantation, here we have established that TRMs have a critical role in early tumour progression (Extended Data Fig. 7e). We show that TRMs accumulate close to tumour cells soon after tumour cells seed the lung tissue, and induce an EMT program that promotes cell invasiveness, while also promoting a T_{reg} cell response that protects tumour cells from killing by $CD8^+$ T cells. These results demonstrate that TRMs provide an ideal niche

for early cancer progression, and identify TRMs as a potential target for the prevention or treatment of early NSCLC lesions.

Online content

Any methods, additional references, Nature Research reporting summaries, source data, extended data, supplementary information, acknowledgements, peer review information; details of author contributions and competing interests; and statements of data and code availability are available at https://doi.org/10.1038/s41586-021-03651-8.

1. Lavin, Y., Mortha, A., Rahman, A. & Merad, M. Regulation of macrophage development and function in peripheral tissues. *Nat. Rev. Immunol*. **15**, 731–744 (2015).
2. Mantovani, A., Marchesi, F., Malesci, A., Laghi, L. & Allavena, P. Tumour-associated macrophages as treatment targets in oncology. *Nat. Rev. Clin. Oncol*. **14**, 399–416 (2017).
3. Ginhoux, F. et al. Fate mapping analysis reveals that adult microglia derive from primitive macrophages. *Science* **330**, 841–845 (2010).
4. Hashimoto, D. et al. Tissue-resident macrophages self-maintain locally throughout adult life with minimal contribution from circulating monocytes. *Immunity* **38**, 792–804 (2013).
5. Schulz, C. et al. A lineage of myeloid cells independent of Myb and hematopoietic stem cells. *Science* **336**, 86–90 (2012).
6. Leader, A. M. et al. CITEseq analysis of non-small-cell lung cancer lesions reveals an axis of immune cell activation associated with tumor antigen load and TP53 mutations. Preprint at https://doi.org/10.1101/2020.07.16.207605 (2020).
7. Martin, J. C. et al. Single-cell analysis of Crohn's disease lesions identifies a pathogenic cellular module associated with resistance to anti-TNF therapy. *Cell* **178**, 1493–1508 (2019).
8. Schneider, C. et al. Induction of the nuclear receptor PPAR-γ by the cytokine GM-CSF is critical for the differentiation of fetal monocytes into alveolar macrophages. *Nat. Immunol*. **15**, 1026–1037 (2014).
9. Xue, W. et al. Response and resistance to NF-κB inhibitors in mouse models of lung adenocarcinoma. *Cancer Discov*. **1**, 236–247 (2011).
10. Zilionis, R. et al. Single-cell transcriptomics of human and mouse lung cancers reveals conserved myeloid populations across individuals and species. *Immunity* **50**, 1317–1334 (2019).
11. Leach, S. M. et al. Human and mouse transcriptome profiling identifies cross-species homology in pulmonary and lymph node mononuclear phagocytes. *Cell Rep*. **33**, 108337 (2020).
12. Sawai, C. M. et al. Hematopoietic stem cells are the major source of multilineage hematopoiesis in adult animals. *Immunity* **45**, 597–609 (2016).
13. Yona, S. et al. Fate mapping reveals origins and dynamics of monocytes and tissue macrophages under homeostasis. *Immunity* **38**, 79–91 (2013).
14. Russell, D. G., Cardona, P. J., Kim, M. J., Allain, S. & Altare, F. Foamy macrophages and the progression of the human tuberculosis granuloma. *Nat. Immunol*. **10**, 943–948 (2009).
15. DuPage, M., Dooley, A. L. & Jacks, T. Conditional mouse lung cancer models using adenoviral or lentiviral delivery of Cre recombinase. *Nat. Protocols* **4**, 1064–1072 (2009).
16. Sutherland, K. D. et al. Multiple cells-of-origin of mutant K-Ras-induced mouse lung adenocarcinoma. *Proc. Natl Acad. Sci. USA* **111**, 4952–4957 (2014).
17. Nieto, M. A., Huang, R. Y., Jackson, R. A. & Thiery, J. P. Emt: 2016. *Cell* **166**, 21–45 (2016).
18. Lim, J. & Thiery, J. P. Epithelial–mesenchymal transitions: insights from development. *Development* **139**, 3471–3486 (2012).
19. Ye, X. et al. Distinct EMT programs control normal mammary stem cells and tumour-initiating cells. *Nature* **525**, 256–260 (2015).
20. Rhim, A. D. et al. EMT and dissemination precede pancreatic tumor formation. *Cell* **148**, 349–361 (2012).
21. Krebs, A. M. et al. The EMT-activator Zeb1 is a key factor for cell plasticity and promotes metastasis in pancreatic cancer. *Nat. Cell Biol*. **19**, 518–529 (2017).
22. Thiery, J. P. Epithelial-mesenchymal transitions in tumour progression. *Nat. Rev. Cancer* **2**, 442–454 (2002).
23. Yang, J. et al. Twist, a master regulator of morphogenesis, plays an essential role in tumor metastasis. *Cell* **117**, 927–939 (2004).
24. Dongre, A. & Weinberg, R. A. New insights into the mechanisms of epithelial–mesenchymal transition and implications for cancer. *Nat. Rev. Mol. Cell Biol*. **20**, 69–84 (2019).
25. Lavin, Y. et al. innate immune landscape in early lung adenocarcinoma by paired single-cell analyses. *Cell* **169**, 750–765 (2017).
26. Tada, Y. et al. Targeting VEGFR2 with Ramucirumab strongly impacts effector/ activated regulatory T cells and $CD8^+$ T cells in the tumor microenvironment. *J. Immunother. Cancer* **6**, 106 (2018).
27. Battaglia, A. et al. Metastatic tumour cells favour the generation of a tolerogenic milieu in tumour draining lymph node in patients with early cervical cancer. *Cancer Immunol. Immunother*. **58**, 1363–1373 (2009).
28. He, F. et al. PLAU inferred from a correlation network is critical for suppressor function of regulatory T cells. *Mol. Syst. Biol*. **8**, 624 (2012).
29. Mucida, D. et al. Reciprocal T_H17 and regulatory T cell differentiation mediated by retinoic acid. *Science* **317**, 256–260 (2007).
30. Soroosh, P. et al. Lung-resident tissue macrophages generate $Foxp3^+$ regulatory T cells and promote airway tolerance. *J. Exp. Med*. **210**, 775–788 (2013).
31. Mizukami, Y. et al. CCL17 and CCL22 chemokines within tumor microenvironment are related to accumulation of $Foxp3^+$ regulatory T cells in gastric cancer. *Int. J. Cancer* **122**, 2286–2293 (2008).
32. Liu, Z. et al. Fate mapping via Ms4a3-expression history traces monocyte-derived cells. *Cell* **178**, 1509–1525 (2019).

[1]Department of Oncological Sciences, Icahn School of Medicine at Mount Sinai, New York, NY, USA. [2]Precision Immunology Institute, Icahn School of Medicine at Mount Sinai, New York, NY, USA. [3]Tisch Cancer Institute, Icahn School of Medicine at Mount Sinai, New York, NY, USA. [4]Division of Hematology and Oncology, Icahn School of Medicine at Mount Sinai, New York, NY, USA. [5]Department of Medicine, Icahn School of Medicine at Mount Sinai, New York, NY, USA. [6]Black Family Stem Cell Institute, Icahn School of Medicine at Mount Sinai, New York, NY, USA. [7]Department of Otolaryngology, Icahn School of Medicine at Mount Sinai, New York, NY, USA. [8]Institut Curie, PSL Research University, INSERM U932, Paris, France. [9]Department of Cancer Immunology, Genentech, South San Francisco, CA, USA. [10]The Ronald O. Perelman Department of Dermatology, New York University Grossman School of Medicine, New York, NY, USA. [11]Experimental Therapies and Novel Biomarkers in Cancer, Hospital La Paz Institute for Health Research (IdiPAZ), Madrid, Spain. [12]Department of Genetics and Genomic Sciences, Icahn School of Medicine at Mount Sinai, New York, NY, USA. [13]INSERM U1218 ACTION, University of Bordeaux, Bordeaux, France. [14]Microscopy CoRE, Dean's CoREs, Icahn School of Medicine at Mount Sinai, New York, NY, USA. [15]Department of Pathology, New York University Grossman School of Medicine, New York, NY, USA. [16]Institute of Thoracic Oncology, Icahn School of Medicine at Mount Sinai, New York, NY, USA. [17]Icahn Genomics Institute, Icahn School of Medicine at Mount Sinai, New York, NY, USA. [18]Human Immune Monitoring Center, Icahn School of Medicine at Mount Sinai, New York, NY, USA. [19]Present address: Cancer Immunity Laboratory, Molecular Oncology Program, Spanish National Cancer Centre, Madrid, Spain. [20]Present address: CeMM, Research Center for Molecular Medicine of the Austrian Academy of Sciences, Vienna, Austria. [21]These authors contributed equally: Erica Dalla, Andrew Leader, Jessica LeBerichel. [22]These authors jointly supervised this work: Julio A. Aguirre-Ghiso, Miriam Merad. ✉e-mail: mcasanova@cnio.es; miriam.merad@mssm.edu

Methods

Data reporting

No statistical methods were used to predetermine sample size. The experiments were not randomized and unless otherwise stated the investigators were not blinded to allocation during experiments and outcome assessment.

Mice

C57BL/6, *Ms4a3-tdTom* reporter and *CD169-DTR* (ref. [33]) male and female mice of 8–12 weeks old were used for tumour experiments (each experiment was sex-controlled). Mice were maintained at specific-pathogen free (SPF) health status in individually ventilated cages at 21–22 °C and 39–50% humidity, under 12-h light–dark cycles. KP mice[15] were generated by crossing *LSL-K-ras*^{G12D} mice (Jackson Laboratories, Jax ID: 008179) with *Trp53*$^{fl/fl}$ mice (purchased from Jackson Laboratories, Jax ID: 008462). *CD169*$^{cre/+}$ mice[34] were donated by P. Frenette and backcrossed to *R26-LSL-tdTomato* (Jackson Laboratories, Jax ID: 007914). Ethical approval for mouse experiments was obtained by the Internal Animal Care and Use Committee at Mount Sinai Hospital.

Fate-mapping

To induce recombination in the *Pdzk1ip1-creER R26Tom/Tom* mice (*Map17*$^{creER/+}$*R26tdTom*), a single dose of 50 mg/kg tamoxifen (Sigma-Aldrich) in sunflower oil was intraperitoneally administered to 4-week-old mice. For continuous labelling experiments *Cx3cr1*$^{creER/+}$*R26YFP* mice were switched onto a chemically defined tamoxifen diet (Envigo; TD.130858) at the appropriate time before tumour injection (4 weeks old) and remained on that diet for the remainder of the experiment.

Diphtheria-toxin-induced depletion of TRMs

Depletion of TRMs was induced by intranasal instillation of 15 ng per mouse of diptheria toxin (DT, List Biological Laboratories).

Tumour implantation

KP cells were grown in complete medium (RPMI + 10% FBS + 1% P/S), and 70% confluent cultures were detached using trypsin 0.25% and counted. A total of 5×10^5 KP or KP-GFP cells were intravenously injected in 1× phosphate-buffered saline (PBS) into the tail vein and allowed to form tumour foci for 5 to 30 days before the lungs were collected. B16-BFP-F10/OVA cells were grown in complete medium (RPMI + 10% FBS + 1% P/S); 5×10^5 B16-BFP-F10/OVA cellswere injected via the tail vein and tumours were analysed 2 weeks after tumour cell injection.

Flow cytometry and FACS

Single-cell suspensions were obtained from lung, lymph nodes and spleen by digestion with collagenase IV (0.25 mg/ml) (Sigma) at 37 °C for 30 min (lung) or 15 min (lymph nodes and spleen) followed by passing through a 70-μm cell strainer and lysis of red blood cells (RBC lysis buffer, BioLegend) for 2 min at room temperature. For flow cytometry or FACS, cells were stained in FACS buffer (PBS supplemented with 10% BSA and 2 mM EDTA) with rat monoclonal antibodies (Supplementary Table 6).

For intracellular staining, cells were fixed with either BD Fix/Perm (for intracellular cytokine stains) or Invitrogen Fix/Perm (for nuclear stains) according to the kit instructions. For T cell cytokine stains, cells were incubated with 1 μg/ml brefeldin A, 1 μg/ml ionomycin and 50 ng/ml PMA (all Sigma) for 4 h at 37 °C followed by staining and fixation. For FACS, cells were prepared and stained as described and sorted on a BD FACSAria. Absolute numbers were calculated using fluorescent beads (Accucheck Counting Beads PCB100, Molecular Probes) following the manufacturer's instructions. Flow cytometry data were acquired using FACS Diva software v.7 (BD).

ATAC–seq primary data processing

Mouse assembly version mm10/NCBI m38 was used for sequence alignments with Bowtie[35] v.2.3.4.1. Sequences with MAPQ scores <30 were removed with SAMtools v.1.9[36] and duplicates were removed with picard-tools v.1.88 (http://broadinstitute.github.io/picard). Integrative Genome Viewer (IGV) viewer files were generated with igvtools v.2.4.1, count -z 5 -w 25 -e 250. ATAC–seq peaks were called with MACS[37] v.2.1.0 with the parameters -q 0.001 –nomodel –extsize 73 –shift -37. For statistical analyses, we generated a sorted list of ATAC–seq peaks containing all experimental conditions and replicates, before we defined read counts for each peak in each condition with HTSeq, and analysed these datasets with DESeq2[38] using $P < 0.05$ as the significance cut-off. Each experimental condition contained three biological replicates. DeepTools[39] was used to generate normalized bigwig files[40] and heat maps to visualize the average enrichment of ATAC signal over the indicated conditions and cluster regions normalized to the effective genome size (mm10). ATAC–seq peaks were analysed with GREAT (Genomic Regions Enrichment of Annotations Tool)[41] using default parameters to calculate the genes associated to ATAC–seq peaks, and AmiGO was used to define Gene Ontology categories enriched in each condition. IGV[42] was used for track visualization.

ATAC–seq

ATAC–seq was performed as described previously[43]. A total of 50,000 FACS-sorted TRMs per sample were spun down at 1,500 r.p.m. for 5 min at 4 °C and washed once with 50 μl of cold PBS. Cells were lysed and incubated for 30 min at 37 °C with 50 μl of transposase reaction, which contained 25 μl of Tagment DNA buffer (Illumina), 2.5 μl of Tagment DNA enzyme (Illumina), 0.5 μl of NP-40 and 7 μl of nuclease-free water. The transposed DNA was immediately purified with the Qiagen MinElute PCR purification kit according to the manufacturer's instructions and eluted in a 10-μl volume. PCR amplification of the transposed DNA was done with a low-cycle-number protocol and with published primers[43]. Each PCR mix contained 25 μl of NEB 2× PCR mix (New England BioLabs), 2.5 μl of 25 μM forward primer (Primer Ad1_noMX), 2.5 μl of 25 μM reverse barcoded primer, 12 μl of water and 8 μl of transposed DNA. PCR was carried out with the following cycling protocol: 72 °C for 5 min; 98 °C for 30 s; and five cycles of 98 °C for 10 s, and 72 °C for 1 min and 39 s. The reaction was held at 4 °C after the fifth cycle.

We set up a side quantitative PCR (qPCR) using the PCR product from these five cycles of amplification. Each qPCR mix contained 7.5 μl of NEB 2× PCR mix, 0.75 μl of 25 μM forward primer, 0.75 μl of 25 μM reverse barcoded primer, 0.1 μl of 100× SYBR Green, 0.9 μl of nuclease-free water and 5 μl of the PCR-amplified product. qPCR was carried out with the following cycling protocol: 98 °C for 30 s; 25 cycles of 98 °C for 10 s, and 72 °C for 1 min and 30 s; and plate reading. The qPCR amplification plot was then used to calculate the additional number of cycles needed for the PCR to achieve the maximum amount of product without going into saturation. Each sample was amplified for a total of 11 cycles. The amplified libraries were then purified with the Qiagen MinElute PCR purification kit according to the manufacturer's instructions and eluted in a 10-μl volume. Libraries were sequenced on a Illumina NextSeq 500 for an average of 10 million paired-end reads per sample.

Ultra-low-input RNA-seq

RNA isolation from 20,000 FACS-sorted TRMs was done with the Qiagen RNeasy micro kit. One nanogram of RNA was synthesized into cDNA using the Smart-Seq v4 Ultra Low Input RNA Kit for Sequencing (Takara Bio). Sequencing libraries were prepared using the Low Input Library Prep Kit (Takara Bio). Libraries were sequenced on an Illumina NextSeq 550 System. FASTQ files were aligned to the mm10 reference genome, reads were dereplicated for PCR duplicates and gene counts were generated using STAR v.2.5 using quantMode GeneCounts. Differential expression analysis was performed with the limma package in R.

Study participants

The patients with lung cancer, specimen acquisition and processing and scRNA-seq and analysis of human samples are described elsewhere[6]. In brief, tumour and non-involved lung resection specimens were obtained from patients undergoing surgery at the Mount Sinai Medical Center in collaboration with the Biorepository and Department of Pathology and under the provisions of a protocol reviewed and approved by Mount Sinai's Institutional Review Board (IRB HS 10-00472 and HS 00135). Informed consent was obtained from the participants. Tissues were rinsed in PBS, minced and incubated for 40 min at 37 °C in collagenase IV 0.25 mg/ml, collagenase D 200 U/ml and DNase I 0.1mg/ml (all Sigma). Cell suspensions were aspirated through a 18G needle 10 times and strained through 70-µm mesh before RBC lysis. Suspensions were enriched for immune cells by magnetic-bead positive selection of $CD45^+$ cells (Miltenyi) before processing for scRNA-seq. A detailed unsupervised analysis of the human scRNA-seq dataset has been published elsewhere[6].

scRNA-seq of KP tumours and naive lungs from mice

For each mouse scRNA-seq sample, 8,500 monocytes and macrophages were sorted as $CD45^+LIN^-$ (CD3/CD19/NKP46) $CD11B^+LY6G^-$ (Extended Data Fig. 1a, c) and encapsulated using the 10X Chromium 3′ v2 chemistry kit according to the manufacturer's instructions. Sequencing libraries were prepared according to the manufacturer's instructions. Quality control of cDNA and final libraries was performed by CyberGreen qPCR library quantification assay (KAPA). Samples were sequenced on an Illumina Nextseq 550 using the 75-cycle kit to a depth of 100 million reads per library.

scRNA-seq of tumour and naive lung from patients with NSCLC

A dataset of scRNA-seq of immune cells from 35 patients with NSCLC that was recently published by our laboratory[6] was revisited here to identify conserved features of TRMs found in other human lung datasets and in mouse lung tumours. Human samples were collected by the Cancer Biorepository at Mount Sinai School of Medicine (MSSM).

scRNA-seq analysis

After library demultiplexing, gene-expression libraries were aligned to the mm10 reference transcriptomes and count matrices were generated using the default Cell Ranger 2.1 workflow, using the "raw" matrix output. Cell clustering was performed as previously described[7], using a method that relies on maximum likelihood for selection of an optimal kmeans seed, followed by an estimation-maximization-like procedure until the model converged. For this study, cells with a mitochondrial gene content of less than 25% and more than 800 gene-expression UMIs detected were retained for analysis.

Cross-species comparison

To select genes that were conserved in homologous groups of monocytes and macrophages between human and mouse, we first identified genes that were upregulated above a $\log_2$-transformed fold change threshold of 1.1 between the average expression of each cell type compared to the average expression of all other monocyte and macrophage cells in each species, respectively. Genes were then filtered for those meeting this threshold in homologous cell types in each species. For visualization, cell-type expression levels were subjected to a log-transform and *z*-scaled within each species.

Analysis of an additional public scRNA-seq dataset

scRNA-seq data of tumours from seven patients with NSCLC and KP mouse lung tumours acquired using inDrop[10] and accompanying cluster annotations were downloaded from the Gene Expression Omnibus (GEO) with accession code GSE127465. Variable genes across monocyte and macrophage clusters were computed as previously described[7]. Expression levels of these genes per were used to compute the Spearman correlation between clusters from ref. [10] and those from the present study.

Spheroids

For experimental set-up, 1×10^3 KP-GFP cells were seeded in 400 µl low-serum medium (RPMI + 5% FBS + 1% P/S + 2% Matrigel) in 8-well chamber slides (Falcon 354118) on top of 50 µl of Matrigel (Corning 356231). After 7 days, 5×10^4 TRMs and bone marrow monocytes were added to the chamber's wells, and 10 ng/ml GM-CSF (Peprotech 315-03) and 10 ng/ml M-CSF (Peprotech 315-02) were added to the TRM and bone marrow monocyte culture media, respectively. Three days later, cultures were fixed with 4% paraformaldehyde for 20 min at room temperature.

Quantification of spheroids with invasive protrusions

Images were taken using a Leica DMI8 microscope at 10×/0.25 objective. Quantifications of acquired images were performed using ImageJ[44]. After thresholding the image and generating a binary mask, the plug-in functions Skeletonize (2D/3D) and Analyze Skeleton (2D/3D) were used. The spheroids with branches measured by the software were considered spheroids with invasive protrusions.

Immunofluorescence and imaging. Three-dimensional cultures were permeabilized using 0.5% Triton X-100 in PBS for 10 min. Blocking was done using immunofluorescence wash buffer (130 mM NaCl, 7 mM Na_2HPO_4, 3.5 mM NaH_2PO_4, 7.7 mM NaN_3, 0.1% BSA, 0.2% Triton X-100, 0.05% Tween-20) with 5% normal goat serum (Gibco PCN5000) for 1 h. E-cadherin (BD Biosciences 610181, 1:100), TWIST1 (Millipore ABD29, 1:100) and active β-catenin (Millipore 05-665, 1:100) were used as primary antibodies. AlexaFluor goat-anti-mouse 568 (Invitrogen A11004) and AlexaFluor goat anti-rabbit 647 (Invitrogen A21244) were used as secondary antibodies. Chambers were removed from slides and wells were fixed and mounted with ProLong Gold Antifade Reagent with DAPI (Invitrogen P36931). Imaging was performed using a Leica SPE confocal microscope (objective 40×/1.15 ACS APO) and ImageJ software was used for quantification. For quantification of positive cells in immunofluorescence, a separate threshold was set for each staining (E-cadherin, TWIST and β-catenin). For analysis of TWIST1-positive cells, the Analyze Particle tool was used and particle counts were measured on thresholded images. For quantification of E-cadherin and β-catenin, regions of interest (ROIs) delineating the membrane signal were counted on thresholded images. For the total number of cells per organoid, binary masks were generated for DAPI and the Analyze Particle tool was used to count the number of nuclei per spheroid.

Bulk RNA-seq of KP-GFP spheroids. For spheroid RNA-sequencing and imaging KP-GFP cells were grown in complete medium in 96-well round bottom Ultra-Low Attachment microplates (Corning, 7007) to allow spheroid formation. A total of 2,500 KP-GFP cells were grown alone or mixed with 5,000 TRMs or 5,000 bone marrow monocytes for 7 days. Thirty-two spheroids per condition (KP-GFP, KP-GFP + TRMs and KP-GFP + BMMs) were pooled and dissociated with TrypLE Express (Thermo Fisher Scientific) for 20 min at 37 °C and under agitation. GFP^+ cells were FACS-sorted (BD FACSAria) for RNA extraction.

Spheroid time-lapse imaging. Spheroids were imaged with a robotized microscope placed in an incubator (IncuCyte S3, Sartorius). Green fluorescence and phase contrast images were acquired every 3 h for 7 days. A mask based on the green fluorescence intensity was created to detect the green objects, which are tumour spheroids. The size of the tumours spheroids was quantified using IncuCyte software. For spheroid protrusion imaging, spheroids grown in 8-well chamber slides coated with Matrigel were imaged in a Leica TCS SP8 confocal microscope using a HC PL APO C2 10×/0.40 DRY lens. A multiple-position experiment was set to image 6 different spheroids (6 positions) at a 3-min interval during a lapse of 4 h. Two-channel, *z*-stack (12 steps)

images were acquired for GFP and bright-field using a 488 Argon laser to image the whole volume of the spheroids.

Oncospheres

KP-GFP cells were seeded in 6-well ultra-low attachment plates at a density of 500 cells per well in 1 ml sphere medium (DMEM/F12, 1× B27 supplement (Gibco 17504044), 500 ng/ml hydrocortisone (Lonza CC-4031), 40 µg/ml insulin (Gibco 12585014), 20 ng/ml EGF (Peprotech AF-100-15-A) and 1% P/S). At time of seeding, 5×10^3 TRMs and bone marrow monocytes were added to the wells. GM-CSF (10 ng/ml; Peprotech 315-03) and 10 ng/ml M-CSF (Peprotech 315-02) were added to TRM and BMM culture media, respectively. After 7 days, the number and size of formed KP oncospheres were assessed by imaging with a Nikon Eclipse Ti-S microscope.

Conditioned medium from tTRMs and tMDMs

Sorted 10^5 tTRMs and tMDMs from late lesions (day 30) were plated in 300 µl of complete medium (RPMI + 10%FBS) overnight. Conditioned medium was prepared by centrifugation of macrophage culture supernatants (2,500 rpm, 5 min at 4 °C), aliquoted and kept frozen until running transwell assays.

Transwell assays

A total of 50,000 KP cells were seeded on serum-free medium (RPMI) on 8.0 µm permeable cell culture inserts (PET filters Celltreat 230639). 0.5 ml of FBS-containing conditioned medium was then added into 24-well plates. KP cells were allowed 18 h to transmigrate. Invasion filters were fixed in PFA 4% at room temperature for 20 min and then mounted and stained with DAPI.

Transwell image analysis

An ImageJ macro was written to count the number of nuclei. GFP-positive nuclei was first filtered. Nuclei detection was performed using the Stardist plug-in[45]. The resulting particles were filtered to exclude smaller particles that did not meet the nuclei size criteria.

Bronchoalveolar isolation of lung TRMs and purification of bone marrow monocytes

Bronchoalveolar TRMs were isolated by lavaging the lung of C57BL/6 wild-type mice with 3 ml of plain RPMI. Bone marrow monocytes were isolated using a bone marrow monocyte isolation kit (Miltenyi 130-100-629) according to the manufacturer's instructions.

In vitro naive CD4$^+$ tTRM and tMDM co-cultures

CD4$^+$ T cells were isolated from wild-type spleens using an Easy Step Naive CD4$^+$ T cell Isolation Kit (19765A) following the manufacturer's instructions.

Adoptive transfer of OT-I and OT-II T cells and detection of antigen-specific CD8$^+$ T cells

CD8$^+$ T cells were isolated from spleens and lymph nodes of OT-I transgenic mice (Jackson Laboratories, Jax ID: 003831) and purified using a MagniSort Mouse CD8 Naive T cell Enrichment kit (Invitrogen, 8804-6825-74) following the manufacturer's instructions. A total of 2×10^5 OT-I cells were intravenously injected into wild-type and *CD169-DTR* mice one day before B16-F10-BFP/OVA tumour cell injection. CD4$^+$ T cells were isolated from OT-II transgenic mice (Jackson Laboratories, Jax ID: 004194) and purified using a MagniSort Mouse CD4 Naive T cell Enrichment kit (Invitrogen, 8804-6824-74). A total of 6×10^5 OT-II cells were intravenously injected into wild-type and *CD169-DTR* mice one day before B16-F10-BFP/OVA tumour cell injection.

Immunofluorescence and imaging in lung sections

For OCT-embedded lungs, frozen sections were thawed and permeabilized with 0.2% Triton X-100 for 10 min. Blocking was performed using 10% BSA + 2% normal goat serum in PBS for 1 h. For paraffin-embedded lungs, slides were dehydrated and antigen retrieval was performed in 10 mM citrate buffer pH 6.0. Blocking was done using 5% BSA + 5% normal goat serum in PBS for 1h. Sections were incubated with primary antibodies overnight at 4 °C and the following day with secondary antibodies for 1 h at room temperature. Mounting was done using ProLong Gold Antifade Reagent with DAPI (Invitrogen P36931). Ki67 (eBioscience 14-5698-82, 1:100); cleaved caspase-3 (CST 9661S, 1:100); p27 (CST 3686S, 1:100); ZEB1 (Sigma, HPA027524 1:300); E-cadherin (BD Biosciences 610181, 1:100); TWIST1 (Millipore ABD29 1:100), SIGLECF (clone 1RNM44N Invitrogen 1:200), pan-cytokeratin (GP11, Progen 1:200) and CD45.1 (clone A20, Biolegend AlexaFluor AF488 1:100) were used as primary or directly conjugated antibodies. AlexaFluor goat anti-rat 568 (Invitrogen A11077), AlexaFluor goat anti-rabbit 568 (Invitrogen A11011), AlexaFluor goat anti-rabbit 647 (Invitrogen A21244), AlexaFluor goat anti-rabbit 405 (Invitrogen A31556), AlexaFluor goat anti-mouse 647 (Invitrogen A21235) and AlexaFluor goat anti-guinea pig 488 (Invitrogen A11073) were used as secondary antibodies. Imaging was performed using a Leica SPE confocal microscope and quantification of fluorescence intensity was performed using ImageJ software and ZEN Black Imaging Software (Zeiss).

Histopathology

Tumour quantification was assessed in paraffin-embedded lung slides stained with haematoxylin and eosin. Slides were scanned using an Olympus Digital Scanner and analysed using Panoramic Viewer and QuPath 0.2.2 software.

Multiplexed immunohistochemical consecutive staining on a single slide

Tissues were fixed in 4% formaldehyde for 24 h and embedded in paraffin. Four-millimetre-thick formalin-fixed paraffin-embedded (FFPE) tissue sections on glass slides were baked at 37 °C overnight, deparaffinized in xylene and rehydrated in decreasing concentrations of ethanol. Tissue sections were incubated in citrate buffer (pH 6) for antigen retrieval at 95 °C for 30 min. Tissue sections were incubated in 3% hydrogen peroxide and in serum-free protein block solution (Dako, X0909) before adding primary antibody for 1 h at room temperature. After signal amplification using secondary antibody conjugated to streptavidin-horseradish peroxidase and chromogenic revelation using 3-amino-9-ethylcarbazole (AEC) (Vector Laboratories, SK4200), slides were counterstained with haematoxylin, mounted with a glycerol-based mounting medium (Dako, C0563) and scanned for digital imaging (Leica Biosystems, Aperio AT2 Digital Whole Slide Scanner). B16 lung tumours were pretreated with Melanin Bleach kit (Polysciences, 24909) before immunohistochemistry staining. Then the same slides were successively destained and restained with subsequent antibodies as described previously[46]. The primary antibodies used are included in Supplementary Table 7. ROIs and quantification of FOXP3$^+$ T_{reg} cells, CD4$^+$ and CD8$^+$ T cells were manually selected using QuPath software[47].

Analysis of the distribution of TRMs, CD3$^+$ cells and FOXP3$^+$ cells in KP tumours

TRMs and FOXP3 cells were manually and group-blinded quantified using Fiji (ImageJ). For CD3 and FOXP3 quantification and distribution in tumours an in-house macro was created using ImageJ. Tumoral area was defined manually by the user drawing an ROI based on the GFP signal. CD3 and FOXP3 cells were segmented and their distribution was quantified.

Immunostaining. Lungs were fixed with 4% paraformaldehyde and kept in 1× PBS until the staining and clearing process started. For the staining, the lungs were first permeabilized with permeabilization buffer (1× PBS, 0.2% Triton X-100 (Sigma X100), 0.3M glycine (Sigma G7403) and 20% DMSO (Sigma D8418)) for 24 h at 37 °C. Lungs were blocked for 3

days with blocking buffer (1 PBS, 0.2% Triton X-100, 6% donkey serum and 10% DMSO) at 37 °C. The blocked lungs were washed twice with washing buffer (1× PBS, 0.2% Tween 20 (Calbiochem 655205) and 5 U/ml heparin (Akron Biotech AK3004)) at room temperature for 5 min each time (Ertürk A, 2012). The lungs were stained with directly labelled antibodies in antibody buffer (1× PBS, 0.2% Tween20, 5 U/ml heparin, 3% donkey serum) for 3 days at 37 °C. The lungs were washed 10 times with washing buffer (1× PBS, 0.2% Tween 20, 5 U/ml heparin (AK3004)) at room temperature for 1 h each time. The antibodies were coupled with either Alexa Fluor 432, Alexa Fluor 594 or Alexa Fluor 647 labelling kits (A20182, A20185, A20186) following the manufacturer's instructions. Lungs were imaged using a 20×/0.60 ACS APO objective on a Leica SPE.

Clearing. Previously stained and washed lungs were dehydrated by submerging them in 30%, 50%, 70%, 80%, 96% and 100% tert-butanol, consecutively, for 3 h each. After dehydration the lungs were cleared using FluoClearBABB solution for 12 h. All the buffers were made following previously reported uDISCO protocol (Pan C, 2016). The dehydration and clearing steps were performed at 30 °C, except for the 30% and 50% steps that were performed at room temperature.

Clearing imaging. The whole cleared lungs have been imaged using a custom-made FluoClearBABB compatible 20× objective on an upright confocal SP8 Falcon microscope (Leica) using the Lightning module. A list of antibodies is included in Supplementary Table 8.

Statistical analysis

Results represent mean ± s.e.m., unless otherwise indicated. Statistical significance between groups was determined by unpaired Student's *t*-test or ANOVA plus Bonferroni or Dunnett's correction for multiple comparisons. Statistical analysis was done with GraphPad Prism v.8.0.

Reporting summary

Further information on research design is available in the Nature Research Reporting Summary linked to this paper.

Data availability

All mice sequencing data are publicly available (GEO accession code GSE147671). The human dataset is available at the Sequence Read Archive (SRA) with BioProject accession PRJNA609924. Source data are provided with this paper.

Code availability

The clustering analysis used here is described fully in its source manuscript[6].

33. Miyake, Y. et al. Critical role of macrophages in the marginal zone in the suppression of immune responses to apoptotic cell-associated antigens. *J. Clin. Invest.* **117**, 2268–2278 (2007).
34. Karasawa, K. et al. Vascular-resident CD169-positive monocytes and macrophages control neutrophil accumulation in the kidney with ischemia-reperfusion injury. *J. Am. Soc. Nephrol.* **26**, 896–906 (2015).
35. Langmead, B., Trapnell, C., Pop, M. & Salzberg, S. L. Ultrafast and memory-efficient alignment of short DNA sequences to the human genome. *Genome Biol.* **10**, R25 (2009).
36. Li, H. et al. The sequence alignment/map format and SAMtools. *Bioinformatics* **25**, 2078–2079 (2009).
37. Zhang, Y. et al. Model-based analysis of ChIP–seq (MACS). *Genome Biol.* **9**, R137 (2008).
38. Love, M. I., Huber, W. & Anders, S. Moderated estimation of fold change and dispersion for RNA-seq data with DESeq2. *Genome Biol.* **15**, 550 (2014).
39. Ramírez, F., Dündar, F., Diehl, S., Grüning, B. A. & Manke, T. deepTools: a flexible platform for exploring deep-sequencing data. *Nucleic Acids Res.* **42**, W187–W191 (2014).
40. Sastre-Perona, A. et al. De novo PITX1 expression controls bi-stable transcriptional circuits to govern self-renewal and differentiation in squamous cell carcinoma. *Cell Stem Cell* **24**, 390–404 (2019).
41. McLean, C. Y. et al. GREAT improves functional interpretation of cis-regulatory regions. *Nat. Biotechnol.* **28**, 495–501 (2010).
42. Robinson, J. T. et al. Integrative genomics viewer. *Nat. Biotechnol.* **29**, 24–26 (2011).
43. Buenrostro, J. D., Giresi, P. G., Zaba, L. C., Chang, H. Y. & Greenleaf, W. J. Transposition of native chromatin for fast and sensitive epigenomic profiling of open chromatin, DNA-binding proteins and nucleosome position. *Nat. Methods* **10**, 1213–1218 (2013).
44. Schindelin, J. et al. Fiji: an open-source platform for biological-image analysis. *Nat. Methods* **9**, 676–682 (2012).
45. Schmidt, U., Weigert, M., Broaddus, C. & Myers, G. Cell detection with star-convex polygons. In *International Conference on Medical Image Computing and Computer-Assisted Intervention –MICCAI 2018* (eds Frangi, A. et al.) 265–273 (Springer, 2018).
46. Remark, R. et al. In-depth tissue profiling using multiplexed immunohistochemical consecutive staining on single slide. *Sci. Immunol.* **1**, aaf6925 (2016).
47. Bankhead, P. et al. QuPath: open source software for digital pathology image analysis. *Sci. Rep.* **7**, 16878 (2017).

Acknowledgements This work was supported by an HFSP postdoctoral fellowship (LT000110/2015-L/1) and an AACR–AstraZeneca Immuno-oncology Research Fellowship (20-40-12-CASA) to M.C.-A.; T32 CA078207 to A.L.; F30 CA243210 to S.T.C.; and ANR-10-IDEX-0001-02 PSL and ANR-11-LABX-0043 and Fondation ARC pour la recherche sur le cancer to P.B. This research was supported in part by the Tisch Cancer Institute at Mount Sinai P30 CA196521-Cancer Center Support Grant. We thank the Human Immune Monitoring Center for all the single-cell profiling and epigenetic studies; the Merad laboratory and A. Lujambio for discussions and reagents; the Flow Cytometry and the Imaging Core at Mount Sinai; and the Cancer Biorepository at MSSM for sample acquisition. This work was also supported by National Institutes of Health (NIH)–National Cancer Institute grants CA257195, CA254104, AT011326, AI128949 and R56AI137244 to M.M., who is also a Samuel Waxman Cancer Research Foundation Investigator; CA109182, CA216248 and CA218024 to J.A.A.-G., who is also a Samuel Waxman Cancer Research Foundation Investigator; CA257195, CA254104, AT011326 and AI128949 to B.D.B.; NCI grant T32 CA078207 to E.D.; and NIH grant AG049074 to B.R.

Author contributions M.M. and M.C.-A. conceived the project. M.M., M.C.-A., P.B. and J.A.A.-G. designed the experiments. M.C.-A., E.D., J.A.A.-G. and M.M. wrote the manuscript. A.L., C.C., A.S.-P., E.A.-P., M.D.P. and E.K. performed computational analysis. M.C.-A., E.D., J.N., B.M.M., S.T.C., M.D.P., M.D., A.T., L.T., P.H., B.M. and J.L. performed experiments. B.B. and M.S. provided reagents. M.B. and C.M. performed image analysis of KP tumours. T.M. provided intellectual input and facilitated access to human samples. C.M.S. and B.R. provided *Pdzk1ip1-creER R26Tom/Tom* mice. All authors contributed to manuscript editing.

Competing interests J.A.A.-G. is a scientific co-founder of, scientific advisory board member and equity owner in HiberCell and receives financial compensation as a consultant for HiberCell, a Mount Sinai spin-off company focused on therapeutics that prevent or delay cancer recurrence. M.M. serves on the scientific advisory boards of Compugen Inc., Innate Pharma Inc., Morphic Therapeutic, Myeloid Therapeutics, Celsius Therapeutics and Genenta. M.M. receives funding from Genentech Inc., Regeneron Inc., Boerhinger Ingelheim Inc. and Takeda Inc. M.M. has ownership interest of less than 5% in Compugen Inc., Celsius Therapeutics Inc., Dren Bio Inc., and Asher Bio Inc. B.M.M., M.B. and C.M. declare that they are Genentech/Roche employees.

Additional information
Supplementary information The online version contains supplementary material available at https://doi.org/10.1038/s41586-021-03651-8.
Correspondence and requests for materials should be addressed to M.C.-A. or M.M.
Peer review information *Nature* thanks the anonymous reviewers for their contribution to the peer review of this work.
Reprints and permissions information is available at http://www.nature.com/reprints.

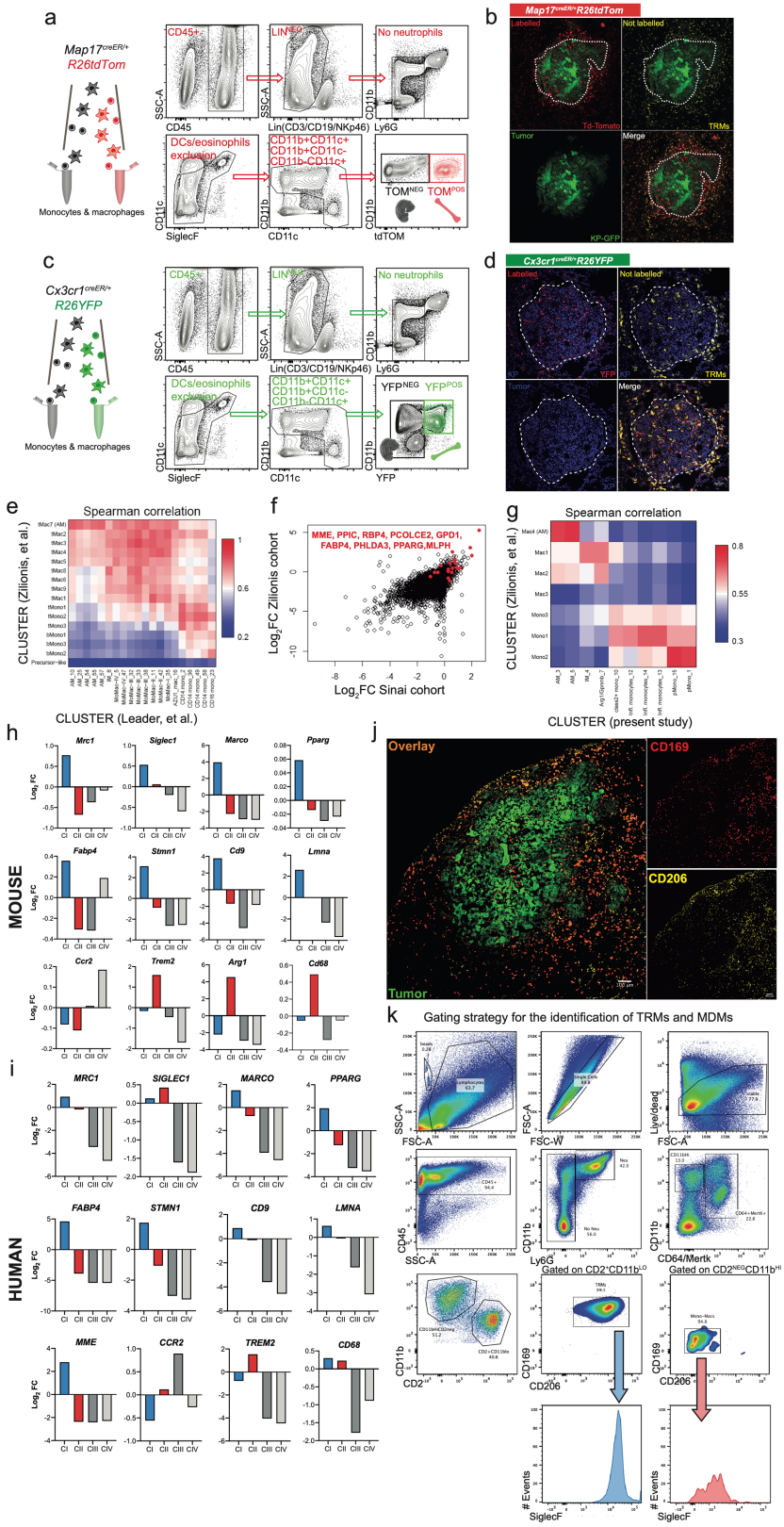

Extended Data Fig. 1 | See next page for caption.

Extended Data Fig. 1 | Macrophage distribution and profile in NSCLC lesions. a, Gating strategy for sorting of myeloid cells from naive and KP tumour-bearing lungs of *Map17*$^{creER/+}$*R26tdTom* mice for scRNA-seq analysis. Monocytes and macrophages in the lung were gated as singlets, DAPI$^-$CD45+Lin$^-$CD11b$^{-/+}$Ly6G$^-$CD11c$^{lo\text{-}int\text{-}+}$SIGLECF$^+$ and Tom$^-$ or Tom$^+$. **b**, Confocal imaging of tdTomato$^+$ bone-marrow-derived leukocytes and TRMs (CD206$^+$, yellow). Images are representative of a single experiment and three tumours imaged. **c**, Gating strategy for sorting of myeloid cells from naive and KP tumour-bearing lungs of *Cx3cr1*$^{creER/+}$*R26YFP* mice. Monocytes and macrophages were gated as in **a** and further separated based on YFP expression. **d**, Confocal imaging of YFP$^+$ bone-marrow-derived leukocytes (red) and TRMs (CD206$^+$, yellow). Scale bar, 50 µm. Images are representative of a single experiment and three tumours imaged. **e**, Spearman correlation of variable gene expression between the human monocyte and macrophage clusters detected in ref. [6] and those in ref. [10]. **f**, The $\log_2$-transformed fold change (FC) between human TRM expression and the maximum cluster expression of non-TRM monocytes and macrophages, determined from data in ref. [6] (*x* axis) or ref. [10] (*y* axis). The human alveolar macrophage genes published previously[11] are highlighted in red. **g**, Spearman correlation of variable gene expression between the mouse monocyte and macrophage clusters detected in the present study and in ref. [10]. **h**, Average expression of selected mouse genes from scRNA-seq data in cluster groups I to IV (see Supplementary Table 2). **i**, Average expression of selected human genes from scRNA-seq data (see Supplementary Table 1). **j**, Confocal imaging of *CD169*$^{cre/+}$*R26tdTom* KP lesions (day 30, KP-GFP, green) with CD206 (yellow). Scale bar, 100 µm. Images are representative of a single experiment and three tumours imaged. **k**, Gating strategy for the identification of TRMs and MDMs in naive lungs. TRMs were gated as live/dead$^-$CD45$^+$Ly6G$^-$CD64$^+$MERTK$^+$CD2$^+$CD169$^+$CD206$^+$SIGLECF$^+$; MDMs were gated as singlets, live/dead$^-$CD45$^+$Ly6G$^-$CD64$^+$Mertk$^+$CD2$^-$CD11b^{hi}CD169$^-$CD206$^-$SIGLECF$^-$.

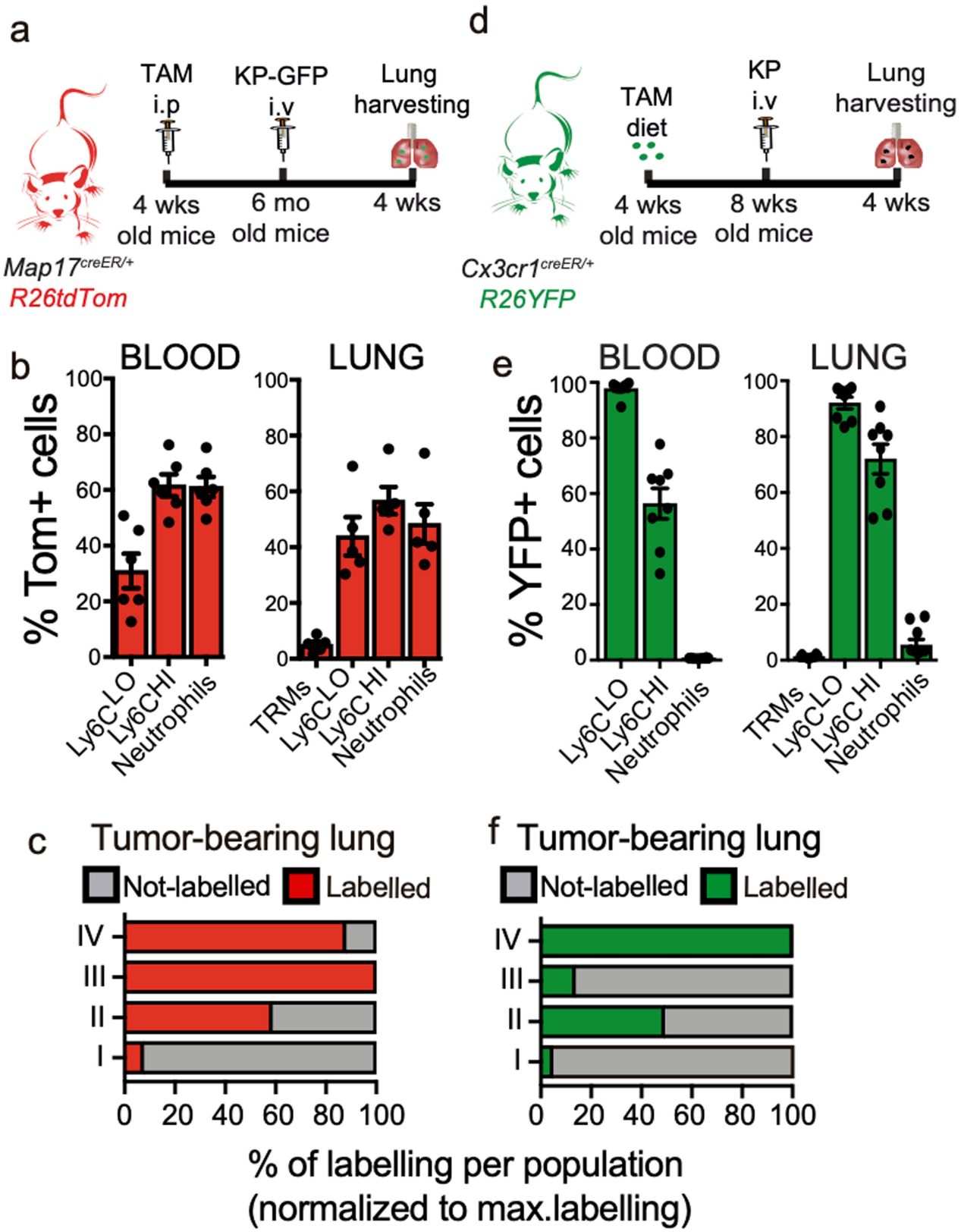

Extended Data Fig. 2 | See next page for caption.

Extended Data Fig. 2 | Fate-mapping of macrophages in KP tumours. **a**, Lineage tracing experiment in *Map17*$^{creER/+}$*R26tdTom* mice. **b**, Fraction of labelled (red, tdTom$^+$) cells in the peripheral blood and lung of non-tumour-bearing *Map17*$^{creER/+}$*R26tdTom* mice 6 months after tamoxifen injection ($n = 6$ blood, $n = 5$ lung; two independent experiments). Blood Ly6C^{hi} monocytes were identified as singlets, DAPI$^-$CD45$^+$CD11b$^+$CD115$^+$Ly6C^{hi} or Ly6C^{lo} monocytes as CD45$^+$CD11b$^+$CD115$^+$Ly6C^{lo}. Lung monocytes were gated as CD45$^+$CD11b$^+$CX3CR1$^+$Ly6C^{hi} or Ly6C^{lo}. Neutrophils in blood and lungs were identified as singlets, DAPI$^-$CD45$^+$CD11b$^+$Ly6G$^+$. TRMs were identified as singlets, DAPI$^-$CD45$^+$Ly6G$^-$CD11b$^{lo/-}$SIGLECF^{hi}CD11c^{hi}CD206^{hi}CD169^{hi}. Data are mean ± s.e.m. **c**, Frequencies of labelled (red, tdTom$^+$) or not labelled (grey, tdTom$^-$) cells within each cluster groups as defined in **b** in tumour-bearing mice. **d**, Lineage tracing experiment in *Cx3cr1*$^{creER/+}$*R26YFP* mice. **e**, Fraction of labelled (green, YFP$^+$) cells in the peripheral blood and lung of non-tumour-bearing mice ($n = 8$, pool of two independent experiments). Data are mean ± s.e.m. **f**, Frequency of labelled (green, YFP$^+$) and non-labelled (grey, YFP$^-$) cells within each cluster groups as defined in **b** in KP tumour-bearing mice.

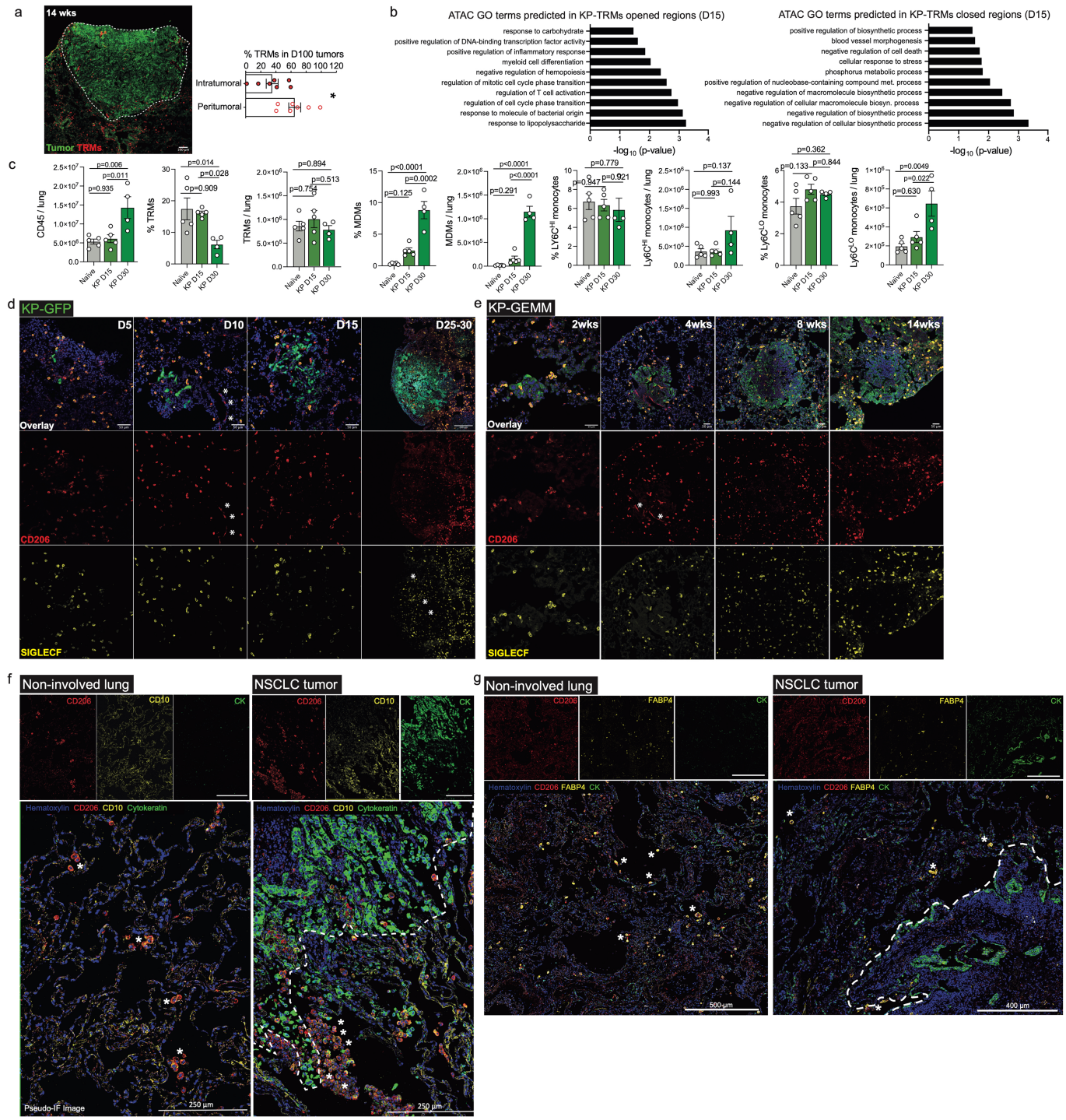

Extended Data Fig. 3 | See next page for caption.

Extended Data Fig. 3 | Longitudinal analysis of TRMs in NSCLC. a, TRMs (red, $CD206^+$) distribution in KP-GEMMs (green) 14 weeks (wks) after injection of adenovirus-$SPC5^{Cre}$ in KP mice. White dotted lines delimit the tumour area. Unpaired two-tailed Student's *t*-test; $^*P = 0.020$. $CD206^+$ macrophage distribution was analysed in $n = 4$ tumour-bearing mice from one experiment. Data are mean ± s.e.m. **b**, Gene Ontology categories for ATAC–seq significant ($P < 0.05$) open (day 15) and closed (day 30) chromatin regions identified in KP-associated TRMs. **c**, Longitudinal analysis of $CD45^+$ leukocytes, TRMs and $Ly6C^{hi}$ and $Ly6C^{lo}$ monocytes in naive ($n = 5$) and in day-15 ($n = 5$) and day-30 ($n = 4$) KP-bearing mice. One-way ANOVA with Tukey's test. Data are mean ± s.e.m. TRMs were gated as singlets, live/$dead^-GFP^-CD45^+Ly6G^-CD64^+MERTK^+CD2^+CD169^+CD206^+Siglecf^+$; MDMs were gated as singlets, live/$dead^-GFP^-CD45^+Ly6G^-CD64^+MERTK^+CD2^-CD11b^{hi}CD169^-SIGLECF^-$. Lung monocytes were gated as $CD45^+CD11b^+CX3CR1^+Ly6C^{hi}$ or $Ly6C^{lo}$. **d**, Longitudinal imaging analysis of TRMs identified by the co-expression of CD206 (red) and SIGLECF (yellow) in the KP-GFP orthotopic model. KP tumour cells, green. White asterisks indicate $CD206^+SIGLECF^-$ macrophages. Yellow asterisks depict $SIGLECF^+CD206^-$ leukocytes, which are also found in overt tumours and are most probably $SIGLECF^+$ eosinophils. Scale bars, 50 µm (D5, D10 and D15); 100 µm (D25–30). Images are representative of one experiment; $n = 3$–5 mice; 2–3 tumours analysed per time point. **e**, Longitudinal imaging analysis of TRMs in the KP-GEMM model. Tumour cells are identified by positive staining with pan-cytokeratin in green. Images are representative of one experiment; 2–3 tumours analysed per mouse; 3 mice per time point. Scale bars, 50 µm. **f**, Immunohistochemistry converted to pseudofluorescence image of CD206 (red), CD10 (yellow) and cytokeratin (CK, green) staining in non-involved lung and NSCLC tissue. White asterisks indicate $CD206^+CD10^+$ TRMs. Scale bars, 250 µm (bottom images); 250 µm (top images). Images are representative of one experiment. **g**, Immunohistochemistry converted to pseudofluorescence image of CD206 (red), FABP4 (yellow) and cytokeratin (CK, green) staining in non-involved lung and NSCLC tissue. White asterisks indicate $CD206^+FABP4^+$ TRMs. Scale bars, 500 µm (left); 400 µm (right). Dotted lines delineate tumour border. Representative images from two non-involved lung and two NSCLC tumours. Images are representative of one experiment.

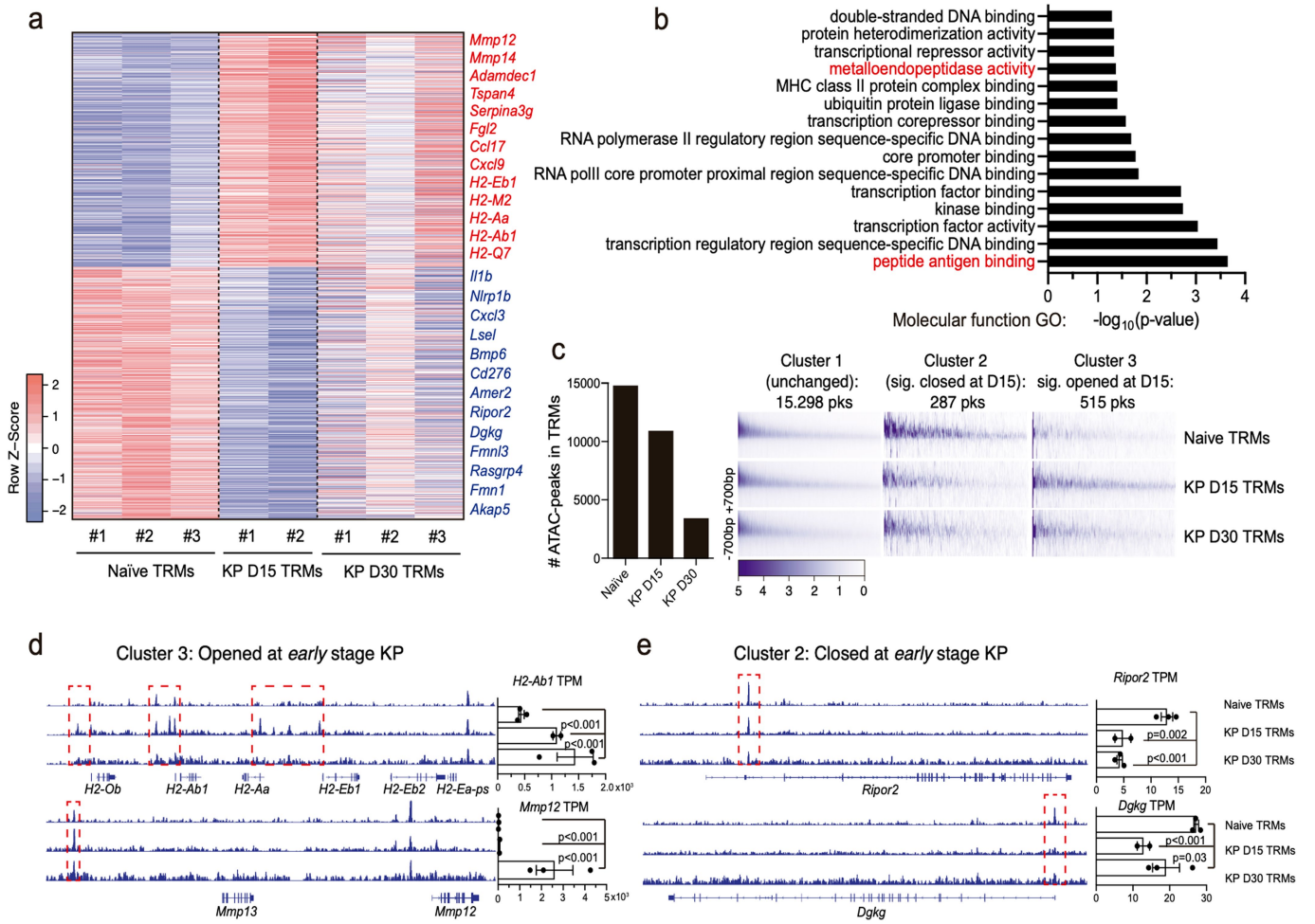

Extended Data Fig. 4 | Bulk RNA-seq and ATAC–seq of KP TRMs. a, Heat map of DEGs of TRMs in naive lungs, day-15 and day-30 KP tumours. Red indicates the most significant upregulated and blue the most significant downregulated gene transcripts ($P < 0.05$, $\log_2$-transformed fold change ($\log_2$FC) > 1 and $\log_2$FC < 1, respectively). TRMs were sorted as singlets, DAPI$^-$CD45$^+$Ly6G$^-$CD11b$^{lo/-}$CD64$^+$MERTK$^+$CD2$^+$CD169$^+$SIGLECF^{hi}CD206$^+$. **b**, Gene Ontology analysis of upregulated DEGs between naive and early KP-TRMs (day 15) ($P < 0.05$ and $\log_2$FC > 1). **c**, Number of peaks and heat map representing average ATAC–seq peaks (pks) unchanged (cluster 1), differentially closed (cluster 2) or opened (cluster 3) in TRMs at different times after KP injection. **d**, **e**, Representative tracks of significant TRM DEGs ($P < 0.05$) showing increased chromatin accessibility (dotted red lines) (**d**) or lower chromatin accessibility (**e**) in TRMs. Tracks are representative of three pooled mice examined over one single experiment. Data are mean ± s.e.m.

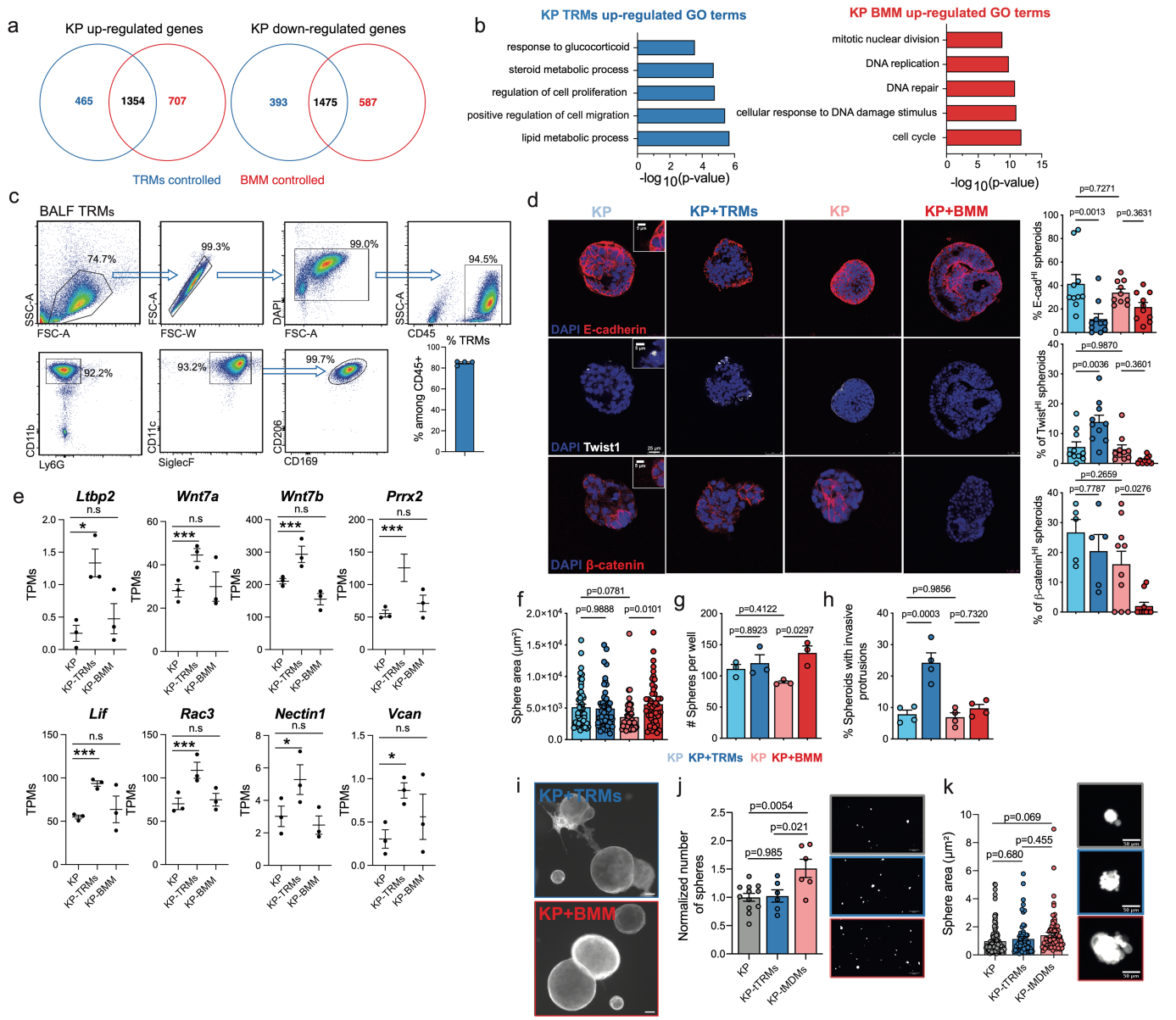

Extended Data Fig. 5 | TRMs promote EMT and a pro-invasive signature in KP spheroids, whereas MDMs favour growth. a, Venn diagrams for DEGs upregulated and downregulated in spheroids co-cultured with TRMs or bone marrow monocytes (BMMs). The number of DEGs uniquely controlled by TRMs or BMMs is shown in blue (TRMs) and red (BMMs). **b**, Gene Ontology (GO) analysis of significant DEGs ($P < 0.05$) with upregulated signature controlled by TRMs (blue) and by BMMs (red), respectively. **c**, Gating strategy for BALF (bronchoalveolar fluid) TRMs gated as $CD45^+CD11b^{lo}CD11c^+SIGLECF^+CD206^+CD169^+$ and purity quantification in $n = 4$ mice. BALF routinely showed around 85% pure TRMs among $CD45^+$ leukocytes. **d**, Confocal representative images and quantification of E-cadherin (red), TWIST1 (white) and β-catenin (red) in KP spheroids cultured alone or with TRMs or BMMs. Scale bars, 5 µm (inset) and 25 µm. One-way ANOVA with Tukey's test. Data are mean ± s.e.m. Two independent experiments. **e**, Bar graphs showing the expression (in transcripts per million, TPM) of EMT-signature selected genes in KP-spheroids alone, with TRMs or BMMs. Data are mean ± s.e.m. Results are representative of one experiment. **f**, Size quantification for KP oncospheres co-cultured with TRMs or BMMs. Data are mean ± s.e.m. Data are representative of two independent experiments. **g**, Quantification of the number of KP oncospheres in co-cultures with TRMs (blue) or BMMs (red) compared to KP alone in the presence of GM-CSF (light blue) or M-CSF (light red), respectively. Data are mean ± s.e.m. Data are representative of two independent experiments. **h**, Quantification of KP 3D-matrigel spheroids with invasive protrusions co-cultured with TRMs or BMMs and their respective controls. Data are mean ± s.e.m. Data are representative of two independent experiments. One-way ANOVA with Tukey's test (**f**–**h**). **i**, Bright-field microscopy images of the spheroids quantified in **h**. Scale bars, 100 µm. **j**, **k**, Number (**j**) and size (**k**) of KP oncospheres cultured alone or co-cultured with tumour-associated tTRMs or tMDMs. Results are representative of two independent experiments analysed using one-way ANOVA. Data are mean ± s.e.m. $^*P < 0.05$, $^{**}P < 0.01$, $^{****}P < 0.0001$.

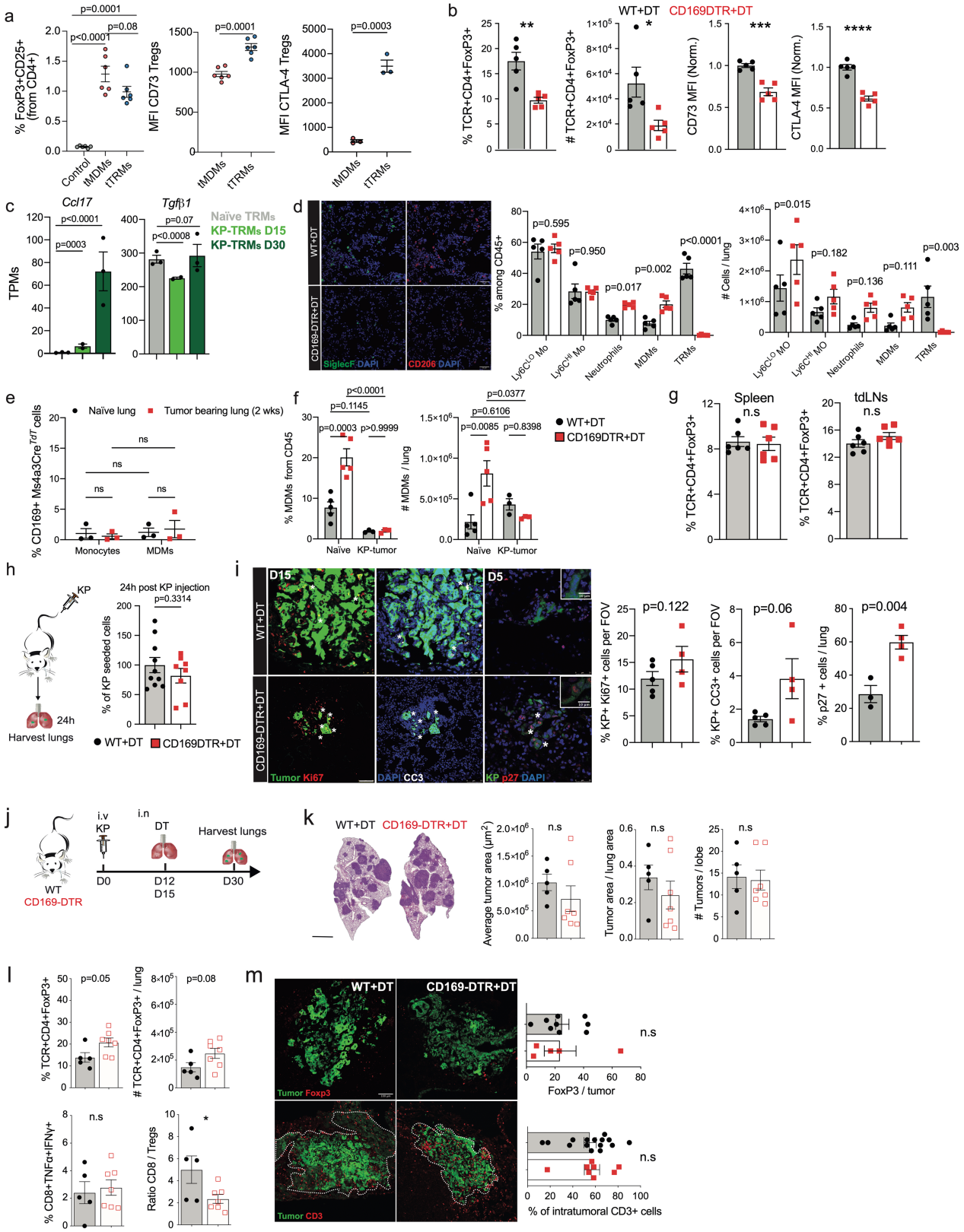

Extended Data Fig. 6 | See next page for caption.

Extended Data Fig. 6 | Immune suppression is governed by TRMs in early KP tumours. a, Frequency, CTLA-4 and CD73 MFI levels of T_{reg} cells induced by tTRMs and tMDMs with naive $CD62L^+CD44^-CD4^+$ T cells (one-way ANOVA with Tukey's test and two-tailed unpaired *t*-test). Two independent experiments. **b**, Frequency and phenotype of T_{reg} cells in TRM-depleted mice at day 15 after KP injection. $n = 5$ mice per group. Two-tailed unpaired *t*-test; $^{**}P = 0.003$, $^{*}P = 0.025$; $^{***}P = 0.0003$ and $^{****}P < 0.0001$, respectively. **c**, Expression of *Ccl17* and *Tgfb1* in TRMs from naive mice (grey) and tumour-bearing mice (day 15 light green, day 30 dark green). Data from DEGs ($P < 0.05$ likelihood ratio test) list in Fig. 2d (see Supplementary Table 3). One experiment, $n = 3$ naive, $n = 2$ KP-TRM day 15 and $n = 3$ KP-TRM day 30 mice. **d**, Imaging of TRM-sufficient and deficient mice after instillation of diphtheria toxin. SIGLECF, green; CD206, red. Quantification of $Ly6C^{hi/lo}$ monocytes, neutrophils, MDMs and TRMs in wild-type or *CD169-DTR* lungs one week after the last dose of diphtheria toxin. $n = 5$ mice per group. Two-tailed unpaired *t*-test. TRMs were gated as singlets, live/dead$^-$CD45$^+$Ly6G$^-$CD64+MERTK$^+$CD2$^+$CD169$^+$SIGLECF$^+$CD206$^+$; MDMs as singlets, live/dead$^-$CD45$^+$Ly6G$^-$CD64$^+$MERTK$^+$CD2$^-$CD11b^{hi}CD169$^-$SIGLECF$^-$; monocytes as CD45$^+$CD11b$^+$CX3CR1$^+$Ly6C^{hi} or Ly6C^{lo} (Ly6C^{hi} and Ly6C^{lo}, respectively); and neutrophils as live/dead$^-$CD45$^+$CD11b$^+$Ly6G$^+$. **e**, Levels of CD169 in Tomato$^+$ monocytes (CD45$^+$CD11b$^+$CX3CR1$^+$) and MDMs (live/dead$^-$CD45$^+$Ly6G$^-$CD64$^+$MERTK$^+$CD2$^-$CD11b^{hi}SIGLECF$^-$) in naive and two-week KP lesions from *Ms4a3-tdTom* reporter mice. $n = 3$ mice per group. Two-way ANOVA with Tukey's multiple comparisons test; ns, not significant. **f**, Frequencies of MDMs in wild-type and *CD169-DTR* lungs after DT treatment with diphtheria toxin in naive mice and KP lesions (two weeks). $n = 5$ per genotype for naive mice and $n = 3$ per genotype for the KP tumour group. Two-way ANOVA with Tukey's multiple comparisons test. **g**, Quantification of T_{reg} cells in spleen and lymph nodes of tumour-bearing mice (day 15) in WT + DT (black) and *CD169-DTR* + DT mice (red). $n = 6$ mice per group. Unpaired two-tailed *t*-test. **h**, Percentage of KP cells from lungs of wild-type or *CD169-DTR* mice treated with diphtheria toxin, 24 h after KP injection. $n = 6$ mice per group. Two-tailed unpaired *t*-test. **i**, Image analysis of Ki67$^+$ and CC3$^+$ KP cells in day-15 lesions, and p27$^+$ KP cells in day-5 lesions of WT + DT and *CD169-DTR* + DT mice. Asterisks show positive KP cells. One-tailed unpaired *t*-test. $n = 3$ WT + DT and $n = 4$ *CD169-DTR* + DT for Ki67 and CC3; $n = 3$ WT + DT and $n = 4$ *CD169-DTR* + DT for p27. Two to three independent experiments. Scale bars, 25 µm (main images); 10 µm (inset). Data are mean ± s.e.m. (**a**–**i**). **j**, Diphtheria toxin treatment and KP injections in wild-type or *CD169-DTR* mice. **k**, Tumour burden in wild-type or *CD169-DTR* mice that were TRM-depleted after tumour implantation. **l**, Quantification of T_{reg} cells, IFNγ$^+$TNF$^+$CD8$^+$ effector cells and ratio of CD8/T_{reg} cells in mice from **k**. Effector T cells were gated as singlets, DAPI$^-$CD45$^+$TCR$^+$CD8$^+$; T_{reg} cells as singlets, DAPI$^-$CD45$^+$TCR$^+$CD4$^+$FOXP3$^+$. $n = 5$ WT + DT and $n = 7$ *CD169-DTR* + DT mice. Three independent experiments. Data are mean ± s.e.m; two-tailed unpaired *t*-test. (**k**, **l**). **m**, Imaging and quantification of infiltrating FOXP3$^+$ T_{reg} cells (top) and CD3$^+$ T cells (bottom) in WT + DT or *CD169-DTR* + DT mice at days 12 and 15 after KP injection. Two-tailed unpaired *t*-test. Data are mean ± s.e.m. Two independent experiments. Scale bar, 100 µm.

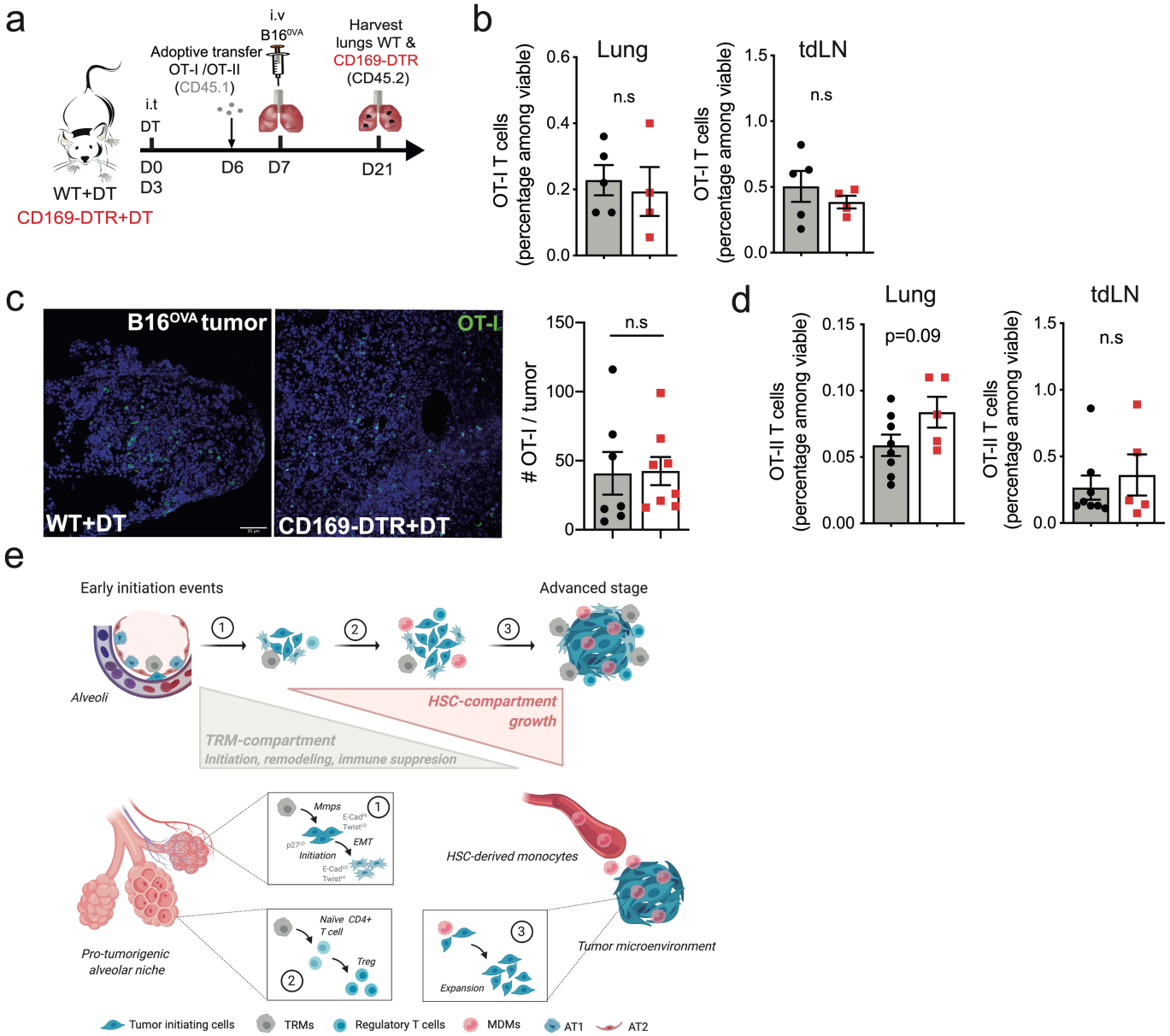

Extended Data Fig. 7 | TRMs modulate T cell effector function in an antigen-independent manner. a, Scheme of OT-I and OT-II adoptive transfer experiments in B16-F10/OVA wild-type and *CD169-DTR* mice. **b**, Relative quantification of OT-I T cells in the lungs and tumour-draining lymph nodes (tdLN). OT-I T cells were gated as viable, CD45.1$^+$TCR$^+$CD8$^+$. $n = 4–5$ mice. Data are representative of two independent experiments. **c**, Quantification of OT-I cells in the tumours of mice in **b**. CD45.1$^+$ OT-I T cells were quantified in 7–8 tumours from mice in **b**. $n = 7$ WT + DT and $N = 8$ *CD169-DTR* + DT from one experiment. Scale bar, 50 µm. **d**, Quantification of OT-II cells in the tumours of mice in **b**. OT-II T cells were gated as viable, CD45.1$^+$TCR$^+$CD4$^+$. $n = 5–8$ mice per group. Data are representative of one experiment. Data are mean ± s.e.m; unpaired two-tailed *t*-test (**b**–**d**). **e**, Scheme of the contribution of the TRM compartment and MDMs to tumour progression. This scheme was created with BioRender.com.

nature research

Corresponding author(s): Maria Casanova-Acebes & Miriam Merad

Last updated by author(s): 04/01/2021

Reporting Summary

Nature Research wishes to improve the reproducibility of the work that we publish. This form provides structure for consistency and transparency in reporting. For further information on Nature Research policies, see Authors & Referees and the Editorial Policy Checklist.

Statistics

For all statistical analyses, confirm that the following items are present in the figure legend, table legend, main text, or Methods section.

n/a	Confirmed	
☐	☒	The exact sample size (*n*) for each experimental group/condition, given as a discrete number and unit of measurement
☐	☒	A statement on whether measurements were taken from distinct samples or whether the same sample was measured repeatedly
☐	☒	The statistical test(s) used AND whether they are one- or two-sided *Only common tests should be described solely by name; describe more complex techniques in the Methods section.*
☒	☐	A description of all covariates tested
☐	☒	A description of any assumptions or corrections, such as tests of normality and adjustment for multiple comparisons
☐	☒	A full description of the statistical parameters including central tendency (e.g. means) or other basic estimates (e.g. regression coefficient) AND variation (e.g. standard deviation) or associated estimates of uncertainty (e.g. confidence intervals)
☐	☒	For null hypothesis testing, the test statistic (e.g. *F*, *t*, *r*) with confidence intervals, effect sizes, degrees of freedom and *P* value noted *Give P values as exact values whenever suitable.*
☒	☐	For Bayesian analysis, information on the choice of priors and Markov chain Monte Carlo settings
☒	☐	For hierarchical and complex designs, identification of the appropriate level for tests and full reporting of outcomes
☐	☒	Estimates of effect sizes (e.g. Cohen's *d*, Pearson's *r*), indicating how they were calculated

Our web collection on statistics for biologists contains articles on many of the points above.

Software and code

Policy information about availability of computer code

Data collection	FACS Diva software version 7(BD), ZEN Black Imaging Software (ZEISS)
Data analysis	FlowJo v10.0.6 (Tree Star Inc.), GraphPad Prism v6.0e (GraphPad Software Inc.), Pannoramic Viewer v1.15.4 (3DHISTECH), ImageJ 2.0.0, and IncuCyte were used for flow cytometry and image analysis. DeepTools, GREAT and IGV v2.5.3 were used to generate ATACseq data. RStudio v1.2, R v3.5.3, R packages: matrixStats, Matrix.utils, mixtools, matrix. tglkmeans (https://tanaylab.bitbucket.io/tglkmeans/) were used for bulk and scRNAseq analysis. Mouse assembly version mm10/NCBI m38 was used for sequence alignments with bowtie version 2.3.4.1. Sequence duplicates in ATACseq were removed with picard-tools version 1.88. Strategies for scRNAseq clustering, cell projection, and homology analyses are similar to previously described approaches (see methods), and scripts are available upon request.

For manuscripts utilizing custom algorithms or software that are central to the research but not yet described in published literature, software must be made available to editors/reviewers. We strongly encourage code deposition in a community repository (e.g. GitHub). See the Nature Research guidelines for submitting code & software for further information.

Data

Policy information about availability of data

All manuscripts must include a data availability statement. This statement should provide the following information, where applicable:

- Accession codes, unique identifiers, or web links for publicly available datasets
- A list of figures that have associated raw data
- A description of any restrictions on data availability

Mouse scRNAseq, ATACseq and bulk RNAseq (Fig. 1a-c; Fig. 2a,d-h; Fig. 3b-c; Extended Data Fig. 1e-h; Extended Data Fig. 2b-c; Extended Data Fig. 3a-b,e) data are all available on GEO (accession number: GSE147671). All human processed gene expression data will be available on GEO, and raw sequencing reads are uploaded to dbGaP, BioProject: PRJNA609924 (GEX, gene expression files on https://dataview.ncbi.nlm.nih.gov/object/PRJNA609924?reviewer=2tal0jn5fi9mm154e8dpk72bnt).

Field-specific reporting

Please select the one below that is the best fit for your research. If you are not sure, read the appropriate sections before making your selection.

☒ Life sciences ☐ Behavioural & social sciences ☐ Ecological, evolutionary & environmental sciences

For a reference copy of the document with all sections, see nature.com/documents/nr-reporting-summary-flat.pdf

Life sciences study design

All studies must disclose on these points even when the disclosure is negative.

Sample size	No statistical methods were used to pre-determine sample size. Sample sizes were estimated based on preliminary experiments, with an effort to achieve a minimum of n=3, mostly n=5 mice per treatment group, which proved sufficient to determine reproducible results.
Data exclusions	For the single-cell RNAseq data, we excluded cells based on pre-established criteria for single-cells, excluded cells with low number of detected transcripts and high mitochondria content. Cell filtering for the human data is described in Leader et al., as noted.
Replication	All experiments were reliably reproduced. All experiments (except for -omics data ie. RNA-seq, ATAC-seq and scRNA-seq) were performed independently at least two times, unless stated (see Figure legends). The ATAC/RNA-seq data from in vivo samples were reliably reproduced, as assessed by Principal Component Analysis (PCA) and hierarchical clustering methods.
Randomization	Mice with matched sex and age are randomized into different treatment groups (eg. naive, tumor). Human subjects were not randomized into experimental groups since we focused on studying macrophage heterogeneity across patients as a whole.
Blinding	Quantification of mouse tumor sizes, lung CC3, Ki67 and p27, CD4, CD8, Treg and CD3 infiltration was blinded by de-identifying samples. In all other experiments, analysis was objective and did not require blinding.

Reporting for specific materials, systems and methods

We require information from authors about some types of materials, experimental systems and methods used in many studies. Here, indicate whether each material, system or method listed is relevant to your study. If you are not sure if a list item applies to your research, read the appropriate section before selecting a response.

Materials & experimental systems

n/a	Involved in the study
☐	☒ Antibodies
☐	☒ Eukaryotic cell lines
☒	☐ Palaeontology
☐	☒ Animals and other organisms
☐	☒ Human research participants
☒	☐ Clinical data

Methods

n/a	Involved in the study
☒	☐ ChIP-seq
☐	☒ Flow cytometry
☒	☐ MRI-based neuroimaging

Antibodies

Antibodies used

The following antibodies were used for flow cytometry:

CD45 (clone 30-F11) BioLegend 1:200 Catalog # 103137
SiglecF (E50-2440) BD Pharmingen 1:200 Catalog # 740956
CD11c (N418) Invitrogen 1:200 Catalog # 47-0114-82
CD24 (M1/69) Invitrogen 1:200 Catalog # 25-0242-82
CD103 (2E7) BioLegend 1:200 Catalog # 17-1031-82
CD11b (M1/70) eBioscience 1:200 Catalog # 45-0112-82
Ly6G (1A8) BioLegend 1:200 Catalog # 127621
Cx3Cr1 (SA011F11) BioLegend 1:200 Catalog # 149037
MHCII I-A/I-E (M5/114.15.2) eBioscience 1:100 Catalog # 12-5321-82
Ly6C (AL-21) eBioscience 1:200 Catalog # 553104
CD206 (Mrc1) (C068C2) BioLegend 1:200 Catalog # 141719
CD169 (3D6.112) BioLegend 1:200 Catalog # 142403
FoxP3 (FJK-16s) Invitrogen 1:100 Catalog # 12-5773-82
TCRb (H57-597) eBioscience 1:200 Catalog # 560657
CD4 (GK1.5) eBioscience 1:200 Catalog # 17-0041-82
CD8 (53-6.7) eBioscience 1:200 Catalog # 558106
IFNg (XMG1.2) eBioscience 1:200 Catalog # 25-7311-41
TNFα (MP6-XT22) eBioscience 1:200 Catalog # 17-7321-82

CTLA-4 (UC10-4B9) eBioscience 1:200 Catalog # 17-1522-82
CD73 (eBioTY/11.8) Invitrogen 1:200 Catalog # 127211
Ki67 (16A8) BioLegend 1:200 Catalog # 652409
CD2 (RM2-5) BioLegend 1:200 Catalog # 100113
Biotin Mertk (Polyclonal) R&D 1:100 Catalog # BAF591
Biotin CD64 (X54-5/7.1) BioLegend 1:100 Catalog # 139318

The following primary antibodies were used for immunofluorescence (IF) and immunohistochemistry (IHC) staining:
E-Cadherin (36/E-Cadherin) BD Biosciences 1:100 Catalog # 610181
Twist1 (Polyclonal) Millipore 1:100 Catalog # ABD29
Active β-catenin (8E7) Millipore 1:100 Catalog # 05-665
Ki67 (SolA15) eBioscience 1:100 Catalog # 14-5698-82
Cleaved Caspase-3 (Asp175) Cell Signaling Technology 1:100 Catalog # 9661S
p27 (D69C12) Cell Signaling Technology 1:100 Catalog # 3686S
SiglecF (1RNM44N) Invitrogen 1:200 Catalog # 14-1702-82
Pan-cytokeratin (Polyclonal) Progen 1:200 Catalog # GP11
CD45.1 (A20) Biolegend 1:100 Catalog # 110717
CD10 (200103) R&D 1:1000 Catalog # MAB1126
CD206 (Polyclonal) Abcam 1:1000 Catalog # ab64693
FABP4 (Polyclonal) R&D 1:100 Catalog # AF1443
Pan-cytokeratin (AE1/AE3) Dako 1:50 Catalog # GA053
FoxP3 (D6O8R) Cell Signaling Technology 1:100 Catalog # 12653
CD4 (EPR195) Abcam 1:1000 Catalog # ab183685
CD8 (4SM15) Invitrogen 1:200 Catalog # 14-0808-82
Pan-cytokeratin (C11) BioLegend 5ug/ml Catalog # 628602
CD206 (C068C2) BioLegend 10ug/ml Catalog # 141702
FoxP3 (FJK-16s) Invitrogen 10ug/ml Catalog # 14-5773-82
CD25 (Polyclonal) R&D 10ug/ml Catalog # AF2438

The following secondary antibodies were used for immunofluorescence (IF) staining:
AlexaFluor goat-anti-mouse 568, Invitrogen 1:1000 Catalog # A11004
AlexaFluor goat anti-rabbit 647, Invitrogen 1:1000 Catalog # A21244
AlexaFluor goat anti-rat 568 Invitrogen 1:1000 Catalog # A11077
AlexaFluor goat anti-rabbit 568 Invitrogen 1:1000 Catalog # A11011
AlexaFluor goat anti-rabbit 405 Invitrogen 1:1000 Catalog # A31556
AlexaFluor goat anti-mouse 647 Invitrogen 1:1000 Catalog # A21235
AlexaFluor goat anti-guinea pig 488 Invitrogen 1:1000 Catalog # A11073
AlexaFluor 432 Catalog # A20182
AlexaFluor 594 Catalog # A20185
AlexaFluor 647 Catalog # A20186

Validation

All the antibodies are validated for the use of immunofluorescence, immunohistochemistry and histological analyses. Data are available on the manufacturer's website. The following primary antibodies have been validated by the manufacturer and;or in this paper:
CD45: Flow cytometric analysis of CD45 expression on mouse splenocytes (website)
SiglecF (BD Pharmingen): Flow cytometric analysis of SiglecF expression on mouse bone marrow leukocytes (website)
CD11c: Flow cytometric analysis of CD11c on expression mouse splenocytes (website)
CD24: Flow cytometric analysis of CD24 expression in mouse splenocytes (website)
CD103: Flow cytometric analysis of CD103 expression on mouse splenocytes (website)
I-A/I-E: Flow cytometric analysis of I-A/I-E expression on mouse splenocytes (website)
CD11b: Flow cytometric analysis of CD11b expression on mouse bone marrow leukocytes (website)
Ly6G: Flow cytometric analysis of LY6G expression on mouse splenocytes (website)
Cx3Cr1: Flow cytometric analysis of CX3CR1 expression on mouse splenocytes (website)
Ly6C: Flow cytometric analysis of CX3CR1 expression on mouse splenocytes (website)
CD206 (BioLegend): Flow cytometric analysis of CX3CR1 expression on mouse splenocytes (website)
CD169: Flow cytometric analysis of CD169 expression on mouse bone marrow leukocytes (website)
FOXP3 (Invitrogen): Flow cytometric analysis of FOXP3 expression on mouse splenocytes (website)
CD4 (eBioscience): Flow cytometric analysis of CD4 expression on mouse splenocytes (website)
CD8 (eBioscience): Flow cytometric analysis of CD8 expression on mouse splenocytes (website)
IFNg: Flow cytometric analysis of IFNg expression on mouse splenocytes (website)
TNFa: Flow cytometric analysis of TNFa expression on mouse splenocytes (website)
CTLA-4: Flow cytometric analysis of CTLA-4 expression on mouse splenocytes (website)
CD73: Flow cytometric analysis of CD73expression on mouse splenocytes (website)
Ki67: Flow cytometric analysis of Ki67 expression on mouse splenocytes (website)
CD2: Flow cytometric analysis of CD45 expression on mouse splenocytes (website)
Biotin Mertk: Flow cytometric analysis of J774A.1 mouse reticulum cell sarcoma macrophage cell line (website)
Biotin CD64: Flow cytometric analysis of CD45 expression on mouse splenocytes (website)
E-Cadherin: Immunofluorescent staining of WIDR cells (website)
Twist1: Immunohistochemistry in ductal breast fibroadenoma and stratified squamous epithelium and cartilage of human trachea tissues (website)
Active β-catenin: Immunocytochemistry, positive staining on the membrane and cytosol (website)
Ki67: Immunohistochemistry on formalin-fixed paraffin embedded mouse skin (website)
Cleaved Caspase-3: Immunohistochemical analysis of paraffin-embedded human tonsil (website)
p27: Immunofluorescent analysis of MCF-7 cells (website)

SiglecF (Invitrogen): Immunohistochemistry of frozen mouse lung (website)
Pan-cytokeratin (Progen): Immunofluorescence staining of mouse CDβGeo cells (website)
CD10: Immunohistochemistry of paraffin-embedded sections of human kidney (website)
CD206 (Abcam): Immunohistochemistry of human lung formalin fixed paraffin embedded tissue section (website)
FABP4: Immunohistochemistry of frozen sections of mouse intestine (website)
Pan-cytokeratin (Dako): Immunohistochemistry of adenocarcinoma (website)
FoxP3 (Cell Signaling Technology): Immunohistochemical analysis of paraffin-embedded 4T1 metastatic tumor in mouse lung (website)
CD4 (Abcam): Immunohistochemistry of mouse colon tissue (website)
CD8 (Invitrogen): Immunohistochemistry of formalin-fixed paraffin embedded mouse spleen (website)
CD25: Immunohistochemistry of immersion fixed frozen sections of mouse spleen (website)

Eukaryotic cell lines

Policy information about cell lines

Cell line source(s)	KP cells were received from Tyler Jacks and B16-BFP/OVA were kindly donated by John Finnigan.
Authentication	Cells were functionally authenticated: KP and B16 cells were injected intravenously into mice and lung tumor progression at different timepoints was followed. No other authentication was performed.
Mycoplasma contamination	All cell lines tested negative for mycoplasma.
Commonly misidentified lines (See ICLAC register)	No commonly misidentified cell lines were used in the study

Animals and other organisms

Policy information about studies involving animals; ARRIVE guidelines recommended for reporting animal research

Laboratory animals	All mice included in this study were analyzed between 8 and 12 weeks of age. Males and females were used in different experiments, each of them sex-controlled. The following mice strains were also included: CD169-Cre R26-LSL-tdTomato, Ms4a3TdT reporter, CD169-DTR, Pdzk1ip1-CreER R26Tom/Tom, C57BL/6, Cx3CR1CreER/+ R26-LSL-YFP, KP-GEMM (SPC-Cre;Trp53fl/fl;LSLKrasG12D), OT-I Tg, OTII-Tg.
Wild animals	The study did not involve wild animals.
Field-collected samples	The study did not involve field-collected samples.
Ethics oversight	Ethical approval for mouse experiments was obtained by the Internal Animal Care and Use Committee at Mount Sinai Hospital.

Note that full information on the approval of the study protocol must also be provided in the manuscript.

Human research participants

Policy information about studies involving human research participants

Population characteristics	Characteristics of the patients analyzed in this study are fully described in Leader et al. Patients were undergoing resection with curative intent of early-stage non-small-cell lung cancer lesions.
Recruitment	Patients over the age of 45 years old were identified and recruited for the study by the surgeons performing the above procedure in collaboration with clinical research coordinators. No self-selection biased was anticipated.
Ethics oversight	The study protocol was approved by the Mount Sinai IRB (study protocols HS# 10-00472 and HS#-00135)

Note that full information on the approval of the study protocol must also be provided in the manuscript.

Flow Cytometry

Plots

Confirm that:

☒ The axis labels state the marker and fluorochrome used (e.g. CD4-FITC).

☒ The axis scales are clearly visible. Include numbers along axes only for bottom left plot of group (a 'group' is an analysis of identical markers).

☒ All plots are contour plots with outliers or pseudocolor plots.

☒ A numerical value for number of cells or percentage (with statistics) is provided.

Methodology

Sample preparation	Single cell suspension was generated from mouse lungs and lymph nodes. Both tissues were minced with scissors prior to digestion with Collagenase IV for 30min (lung) or 15min (lymph node and spleen). The cells were filtered and subjected to red blood cell lysis.
Instrument	BD LSRFortessa
Software	FACS Diva software version 7 (BD)
Cell population abundance	Purity of sorted populations for ATACseq was ~99% in all samples and was assessed by flow cytometry.
Gating strategy	Gating for TRMs: 1. Gate on fsc-a vs. ssc-a was set to include all cell populations, but excluding debris. 2. Gate on fsc-a vs. fsc-w was set to exclude doublets. 3. gate on ssc-a vs. ssc-w was set to exclude doublets. 4. gate on fsc-a vs. live/dead was set to exclude dead cells (live/dead+). 5. gate on CD45+ vs. ssc-a was set to exclude CD45- cells. 6. gate on CD11b+ Ly6G+ was set to exclude neutrophils. 7. gate on CD64-Mertk double positive cells was set to enrich for macrophages, which were further gated as CD11blowCD2+, CD169+, Mrc1+, SiglecF+. Gating for KP-GFP in spheroids: 1. Gate on fsc-a vs. ssc-a was set to include all cell populations, but excluding debris. 2. Gate on ssc-a vs. ssc-h was set to exclude doublets. 3. gate on fsc-a vs. DAPI was set to exclude dead cells (DAPI+). 4. gate on CD45+ vs. GFP+ was set to sort KP-GFP cells (CD45-GFP+).

☒ Tick this box to confirm that a figure exemplifying the gating strategy is provided in the Supplementary Information.